



UNIVERSIDAD NACIONAL AUTÓNOMA DE MÉXICO
PROGRAMA DE MAESTRÍA Y DOCTORADO EN INGENIERÍA
INSTITUTO DE ENERGÍAS RENOVABLES

STUDY OF THE RAYLEIGH-BÉNARD-POISEUILLE FLOW

TESIS

QUE PARA OPTAR POR EL GRADO DE

MAESTRA EN INGENIERÍA

P R E S E N T A

JANETTE ALEJANDRA GARCÍA MORALES

DIRECTOR DE TESIS

DR. RAÚL MAURICIO RECHTMAN SCHRENZEL
Instituto de Energías Renovables

Temixco, Morelos. Febrero 2022

Contents

1	Introduction	8
2	The lattice Boltzmann equation method	12
2.1	Introduction	12
2.2	Boltzmann's transport equation	14
2.3	The equilibrium distribution function $f^{(eq)}$	16
2.4	Discretization of Boltzmann's transport equation	19
2.5	The lattice Boltzmann equation method in the $D2Q9$ model . . .	21
2.6	The temperature field	27
2.7	The Chapman-Enskog expansion	28
2.8	Conclusions	31
3	Heat transfer in solids using the LBEM	32
3.1	Introduction	32
3.2	Heat flux, thermal conductivity and thermal diffusivity	33
3.3	Heat conduction between two solids	38
3.4	Conclusions	41
4	Rayleigh-Bénard-Poiseuille flow	42
4.1	Introduction	42
4.2	Poiseuille flow	45
4.3	Rayleigh-Bénard convection	50
4.4	Rayleigh-Bénard-Poiseuille flow	56
4.5	Conclusions	69
5	Conclusions	71
	Bibliography	74

List of Figures

- 2.1 Schematic representation of the discrete velocity vectors \mathbf{c}_k for the $D2Q9$ model. 24
- 3.1 The heat flux in the vertical direction q_y as a function of time t for different bottom wall temperatures T_H . In the numerical simulations, the number of mesh sites in L_x is $N_x = 51$, the temperature $T'_C = 0.1$ and the relaxation time $\tau_T = 2$ 35
- 3.2 (a) The heat flux q_y in the vertical direction as a function of the temperature gradient in the vertical direction $\Delta T/L_y$ in a steady state for different relaxation times τ_T . The colored continuous lines are the fit of $q_y = k\Delta T/L_y$. (b) The thermal conductivity k as a function of the relaxation time τ_T , open squares in black. The data is fit by $k = 0.33\tau_T$, continuous line in black. 36
- 3.3 The temperature T as a function of the vertical axis y at different times t , colored squares, together with the solution of equation (3.10), shown as the continuous curves in black. The average percentual error for the temperature in a steady state is 0.00334%. In the numerical solutions, $n = 200$, $\alpha = 0.86$, $T_C = 0$, $T_H = 1$ and the number of mesh sites in L_x, L_y is $N_x = 51, N_y = 101$ 37
- 3.4 Scheme of a solid made of two different materials with different thermal diffusivities α_0 and α_1 . The length is L_x , the total height $L_y = L_{y0} + L_{y1}$ with L_{y0} and L_{y1} the heights of the bottom and the top solids respectively. 38

- 3.5 The temperature $T(L_x/2, y)$ as a function of the vertical direction y at different times t together with the interface temperature in a steady state $T_I = 0.364$, horizontal line in black, given by equation (3.17) and the steady state temperature, two straight segments in black, given by equation (3.14). The average percentual error for the temperature in a steady state is 0.65%. In the numerical simulations $T_H = 1$, $T_C = 0$, $\rho c_p = 1$, $\alpha_0 = 0.86$, $\alpha_1 = 1.5$ and the number of mesh sites in L_x, L_y with $L_y = L_{y0} + L_{y1}$ is $N_x = 51, N_y = 101$ 40
- 4.1 Schematic representation of a three dimensional cavity with length L_x , height L_y and width L_z 44
- 4.2 Schematic representation of the two dimensional steady state Poiseuille flow with no-slip boundary conditions in the horizontal walls with length L_x and periodic boundary conditions (PBC's) in the vertical walls with height L_y 45
- 4.3 (a) For $Re = 1,000$, the normalized velocity profiles u/Re as a function of the height y at $x = 1/2$ and several times t together with the solution of equation (4.14), continuous colored curves. The average percentual error of the solutions in steady states is 3.8%. (b) The normalized velocity profile u/Re at $x = 1/2, y = 1/2$ as a function of time t for different Reynolds numbers Re together with the graph of equation (4.14), continuous curve in black. In the numerical solutions, $n = 200$, $\tau = 0.6$, $\rho = 1$, the number of mesh sites in L_y is $N_y = 101$ 49
- 4.4 Schematic representation of the Rayleigh-Bénard convection. The cavity has length L_x and height L_y with $L_x = L_y/2$. The acceleration due to gravity g points vertically downwards. The bottom and top walls are at constant temperatures T_H and T_C , respectively, with $T_H > T_C$ 50

- 4.5 (a) The maximum vertical velocity v_{max} as a function of time t for different Rayleigh numbers Ra . The colored continuous curves are the fit of $v_{max} = A \exp(\gamma t)$. (b) The growth rate of the maximum vertical velocity γ as a function of the Rayleigh number Ra for different relaxation times τ . For $\tau = 0.6$, the Rayleigh number $Ra = 1,707.75$, is shown as the vertical dotted line. In the numerical simulations $\rho = 1$, $\tau = 0.6$, $Pr = 0.71$ and the number of mesh sites in L_x, L_y is $N_x = 201, N_y = 101$ 53
- 4.6 The temperature field and the isotherms in steady states for three values of Ra . (a) $Ra = 2 \times 10^3$, (b) $Ra = 2 \times 10^5$ and (c) $Ra = 1 \times 10^6$. There are 10 isotherms between $0 \leq T \leq 1$ 54
- 4.7 The steady state Nusselt number Nu as a function of the Rayleigh number Ra . The Nusselt number grows as $Nu = aRa^b$ with $a = 0.198$ and $b = 0.28$. The LBEM simulations, open circles in magenta, agree with the results of Shan for large Ra , black curve [1], and those of Clever and Busse, green crosses [2]. In both cases, the percentual error is less than 4% for $5,000 \leq Ra \leq 50,000$ 55
- 4.8 Schematic representation of the Rayleigh-Bénard-Poiseuille (RBP) flow. The cavity has a length L_x and a height L_y with $L_y = L_x/2$. The fluid is driven by a pressure difference in the x direction and a temperature difference in the y direction. The bottom temperature T_H and the top temperature T_C with $T_H > T_C$. The acceleration due to gravity g points vertically downwards. 56
- 4.9 The horizontal component of the velocity u as a function of the height y together with the steady state solution of Poiseuille flow, shown as the continuous curve in black, given by equation (4.13). (a) The horizontal velocity u as a function of y in a periodic steady state for Reynolds number $Re = 10$ and different Rayleigh numbers Ra . (b) The horizontal velocity u as a function of y for $Ra = 2,000$, $Re = 10$ and different times t . In terms of dimensional variables, the parameters are $N_x = 201$, $N_y = 101$, $\rho = 1$, $\tau = 0.6$, $Pr = 0.71$, $\beta = 0.1$ and $g = 0.001$. We keep these values for most of the numerical simulations, except where noted. 59

- 4.10 The velocity fields in periodic steady states in the first column together with the vertical velocity v as a function of the horizontal velocity u in the second column, at $x = 1/2$ and different heights of the cavity y , for Rayleigh number $Ra = 20,000$. (a) and (b) $Re = 5$, (c) and (d) $Re = 50$, (e) and (f) $Re = 150$, and (g) and (h) $Re = 175$ 61
- 4.11 The temperature field and the isotherms in periodic steady states for $Ra = 20,000$ and the same values of Re of the previous figure. There are 20 isotherms between $0 \leq T \leq 1$ 62
- 4.12 The vertical velocity v as a function of the horizontal velocity u at $x = 1/2, y = 1/2$ and $Ra = 20,000$, after a time transient for different values of the Reynolds number Re 63
- 4.13 The Power spectra P as a function of the frequency f for $Ra = 20,000$ and $Re = 50$. The horizontal velocity component u , continuous line in magenta together with the vertical velocity component v , continuous line in green. The fundamental frequencies for u and v are $f_u = 34.42$, shown as the vertical dashed line on the right and $f_v = 17.48$, shown as the vertical dashed line on the left. 64
- 4.14 The fundamental frequency f of the velocity components u and v as a function of the Reynolds number Re for six values of the Rayleigh numbers Ra at $x = 1/2, y = 1/2$. (a) f as a function of Re of the horizontal velocity component u . (b) f as a function of Re for the vertical component v . The fundamental frequency f is fit by $f = mRe$ with $f_u = 2f_v$ 65
- 4.15 The slope of equation (4.26) of the horizontal component of the velocity m_u together with the slope of equation (4.26) of the vertical component m_v as a function of the Rayleigh number Ra 66
- 4.16 The Nusselt number Nu , calculated with equation (4.22), in a steady state as a function of the Reynolds number Re for five values of Rayleigh number Ra 66

- 4.17 The critical Rayleigh number Ra_c as a function of the Reynolds number Re for different mesh sizes. For $Re \leq 50$ the data grows as $Ra_c = aRe^2 + bRe + c$ with $c \approx 1,708$, shown as the dotted curves in black. For $Re \geq 50$ the data grows as $Ra_c = a_1Re^2 + b_1Re + c_1$, shown as the continuous curves in black. (a) For $N_y = 101$ and $Re \leq 50$, $a = 0.43$, $b = -0.43$ and $c = 1708.86$. (b) For $Re \geq 50$, $a_1 = 0.02$, $b_1 = 153.73$ and $c_1 = -8735.6$. (c) For $N_y = 151$ and $Re \leq 50$, $a = 0.43$, $b = -0.41$ and $c = 1,707.85$. (d) For $Re \geq 50$, $a_1 = 0.04$, $b_1 = 143.3$ and $c_1 = -8,056.9$. (e) For $N_y = 201$ and $Re \leq 50$, $a = 0.43$, $b = -0.4$ and $c = 1,707.42$. (f) For $Re \geq 50$, $a_1 = 0.03$, $b_1 = 165.1$ and $c_1 = -12,481.1$ 67
- 4.18 The Nusselt number Nu as a function of the Rayleigh number Ra for four values of the Reynolds number Re . For large values of Ra , Nu grows as $Nu = aRa^b$. For $Re = 0$ with $a = 0.231$ and $b = 0.264$, for $Re = 20$ with $a = 0.233$ and $b = 0.264$, for $Re = 40$ with $a = 0.236$ and $b = 0.261$, and for $Re = 60$ with $a = 0.231$ and $b = 0.263$ 68

Acknowledgments

First of all, I would like to thank the Mexican National Council on Science and Technology (CONACyT) for granting me an scholarship that gave me the opportunity to pursue my postgraduate studies.

I would like to thank for the partial economic support from project IN112719 PAPIIT-DGAPA-UNAM.

I am grateful to the Instituto de Energías Renovables de la Universidad Nacional Autónoma de México (IER-UNAM) and all its member's staff for providing such a stimulating place to study and work in.

I want to express my sincere gratitude to my supervisor Dr. Raúl Rechtman, for his friendship, patience, the frequent meetings and the immense knowledge. You provided me with valuable open source tools to successfully complete this thesis.

I would like to offer my special thanks to my committee members, Dr. Eduardo Ramos for his trust and support, Dr. Guillermo Barrios who introduced me to the world of Python, Dr. Francisco Mandujano and Dr. Jorge Rojas for your comments and suggestions.

Finally, my deepest love and gratitude to my family, specially to my dad and Socorro, and to my partner Marek. I truly appreciate your encouragement, love and support. I also appreciate all the unconditional support I received from my classmates and friends.

Chapter 1

Introduction

In this thesis, we use the lattice Boltzmann equation method (LBEM) in the $D2Q9$ to study the Rayleigh-Bénard-Poiseuille flow with the double distribution function model. To test the accuracy of the LBEM to simulate fluid flows with heat transfer, we carried out numerical simulations for two heat conduction problems, Poiseuille flow and Rayleigh-Bénard convection. We compare our results with theoretical solutions and available data.

The Rayleigh-Bénard-Poiseuille flow (RBP) is described by the competition of two body forces, the buoyancy force generated by a temperature difference in the vertical direction and a pressure gradient in the horizontal direction. These two problems are known as the Rayleigh-Bénard convection, characterized by the Rayleigh number Ra , and the Poiseuille flow, characterized by the Reynolds number Re . Ra is proportional to the temperature difference between the lower and upper horizontal walls of the cavity and Re is proportional to a representative velocity. For any value of Re and for Ra beyond the critical Rayleigh number Ra_c , two different instabilities appear, the transversal rolls and the longitudinal rolls. The transversal rolls are perpendicular to the flow direction and are two dimensional structures [3]. The longitudinal rolls are parallel to the flow direction and appear in some conditions in a three dimensional domain [4].

The aim is to determine the critical Rayleigh number Ra_c as a function of Re to study the transition from the transversal rolls or RBP flow to the conductive state characterized by the Poiseuille flow, for large values of Re and Ra . This transition is determined by measuring the Nusselt number Nu in the vertical direction in a steady state as a function of Re .

The LBEM is a powerful numerical method to simulate flows with heat transfer [1, 5, 6, 7, 8, 9]. This method is originated from the lattice gas cellular automata (LGCA). The LGCA simulate a fluid flow with a particle system that evolves in two steps, propagation and collision, where space, time and velocities are discrete. The set of discrete velocities are defined by the geometry of the lattice. The system evolves due to a set of collision rules where mass and momentum are conserved. Hardy, Pomeau and Pazzis [10] presented the first and simplest model of a LGCA called HPP. Frisch, Hasslacher and Pomeau [11] presented a model called FHP that considered the geometry of the lattice to recover the Navier-Stokes equations. Instead of a set of discrete variables, McNamara and Zanetti [12] proposed the average of the population of the particles which evolution depends on the Boltzmann transport equation (BTE). Bhatnagar, Gross and Krook (BGK) [13, 14] proposed to replace the collision integral of the BTE by a relaxation to the local equilibrium term yielding to the lattice Boltzmann equation method in the BGK approximation. Several authors [7, 9, 15] have shown that the Navier-Stokes equations can be recovered by the Chapman and Enskog expansion.

The two dimensional Rayleigh-Bénard-Poiseuille flow for air ($Pr = 0.71$) inside a rectangular cavity has been studied by several authors. The first numerical and experimental studies were presented by Ouazzani et al. [16] for $2,000 \leq Ra \leq 12,000$ and $1 \leq Re \leq 9$. Müller et al. [17] compared their numerical results with theoretical results for low values of Re and Ra . Many authors reported correlations for the Nusselt Nu and Rayleigh Ra numbers for small values of Ra with cavities filled with air [18, 19, 20, 21]. Nicolas et al. [4] studied the bidimensional RBP flow for water ($Pr = 6.4$) for $Ra \leq 6,000$ and $Re \leq 3$. Their results showed that for $Re < 0.26$, the transversal roll frequency as a function of the Reynolds number decreases when the Rayleigh number increases. Beyond this value, the frequency increases as a function of the Rayleigh number.

The Poiseuille flow is stable below the critical Rayleigh number Ra_c . For larger values of Ra_c , two instabilities are observed, the transversal rolls and the longitudinal rolls. The transversal rolls appear only in a

bidimensional domain while the longitudinal rolls can be observed only in a three dimensional domain [4, 16, 17].

Numerical and experimental studies for three dimensional RBP flow have been carried out by several authors [3, 22, 23, 24, 25]. Schröder and Bühler [25] studied the RBP flow for silicon oil ($Pr = 530$), Rayleigh numbers $2,300 \leq Ra \leq 20,000$ and Reynolds numbers $3 \times 10^{-5} \leq Re \leq 0.1$. They found that the transversal roll frequency as a function of the Reynolds number increases with Ra . At $Ra > 14,000$, the frequency varies slightly due to the convective motion barely affects the traveling velocity. Fujimura and Kelly [22] documented that at high Reynolds numbers, the longitudinal rolls interact with a tranverse traveling wave known as Tollmien-Schlichting wave for $Re > 140$ and $Pr = 1$. The study of the RBP flow has several technological and industrial applications, for instance, the cooling of electronic components [26], the study of a flow inside solar chimney power plants [27] or the study of the chemical vapor deposition (CVD) which is a technique to manufacture thin films such as solar cells [28].

In chapter 2 section 2.2, we present the Boltzmann's transport equation which describes the irreversible relaxation towards equilibrium in an isolated system. In section 2.3, we show the equilibrium distribution function given by the Maxwell-Boltzmann distribution function and its approximations to low Mach numbers. In section 2.4, we present the BGK approximation for the collision term, here the collision integral is replaced by a relaxation to the local equilibrium term and we discuss the discretization in time of this approximation. In sections 2.5 and 2.6, we obtain the hydrodynamic moments of the equilibrium distribution function $f^{(eq)}$, we discuss the discretization of the phase space and we obtain the LBEM in the $D2Q9$ model for the velocity and temperature fields. In section 2.7, we obtain the mass, momentum and energy conservation equations of fluid dynamics from the BTE through a Chapman and Enskog expansion.

In chapter 3, we show that heat transfer problems in solids can be simulated by the $D2Q9$ LBEM with the temperature distribution function. To test our results, we study the heat conduction in solids and compare our results with analytic solutions. In section 3.2, we study the heat conduction in a two dimensional solid that is heated from below. We calculate the heat flux in the vertical direction as a function of time. From Fourier's law,

we find a relation between the relaxation time for the temperature field and the thermal conductivity. We compare the numerical results with the solution in steady and non-steady states. In section 3.3, we present the heat transfer in a bidimensional block made of two solids, one on the top of the other with different thermal diffusivities. We compare our results with the analytic solution and the interface temperature solution in steady states.

In chapter 4 section 4.2, we study the Poiseuille flow. We compare our numerical results with the analytic solution in steady and non-steady states. In section 4.3, we simulate the Rayleigh-Benard convection with the double distribution function model. We validate our simulations by comparing the results with those of Shan [1], and Clever and Busse [2]. In section 4.4, we simulate the two dimensional Rayleigh-Bénard-Poiseuille flow for air. We find that for Rayleigh numbers beyond the critical Rayleigh number and $Re > 0$, the Poiseuille flow breaks the symmetry of the convection rolls and they move downstream to the right. In a steady state, the velocity components u and v are closed and there is a symmetry between their trajectories at $L_y = 1/4$ and $L_y = 3/4$ with L_y the height of the cavity. The components of the velocity u and v at any point $(x, L_y/2)$ oscillates in time in a way that the frequency of u is twice that of v . The Nusselt number as a function of the Reynolds number shows that for fixed Ra , the transition from Poiseuille to RBP flow is found when the Nusselt number $Nu = 1$. As Ra grows, we find a transition at a critical value of the Rayleigh number Ra_c where the flow is the RBP flow. We find the transition curve by plotting Ra_c as a function of Re for different cavity sizes. For the largest cavity size, the Rayleigh and Reynolds numbers $Ra \leq 300,000$ and $Re \leq 1,500$, respectively. Finally, we find that Nu as a function of Ra grows as a power law for large values of Ra .

In chapter 5, we present the conclusions of this thesis.

Chapter 2

The lattice Boltzmann equation method

2.1 Introduction

In this chapter, we present an overview of the lattice Boltzmann equation method (LBEM) which is a useful numerical tool to simulate different fluid flows. The LBEM is a numerical method for solving the Boltzmann's transport equation (BTE) for the velocity distribution function. The Navier-Stokes equations can be recovered through a Chapman and Enskog expansion [15, 7]. The BTE was presented in 1872 by Ludwig Boltzmann. This equation describes the irreversible relaxation towards equilibrium in an isolated system. In section 2.2, we discuss the velocity distribution function and we present the BTE. In section 2.3, we introduce the Maxwell Boltzmann's distribution function, also known as the equilibrium distribution function $f^{(eq)}$ and its low Mach number approximation up to the second order. In section 2.4, we present the Bhatnagar, Gross and Krook (BGK) approximation, here the collision integral is replaced by a relaxation to the local equilibrium term and we discuss the discretization in time of this approximation. In sections 2.5 and 2.6, we obtain the hydrodynamic moments of the equilibrium distribution function $f^{(eq)}$, we discuss the discretization of the phase space

and we obtain the LBEM in the $D2Q9$ model for the velocity and the temperature fields. In section 2.7, we obtain the mass, momentum and energy conservation equations of fluid dynamics from the BTE through a Chapman and Enskog expansion. In section 2.8, we end with some conclusions.

2.2 Boltzmann's transport equation

Let us consider a dilute gas with N particles contained in a cavity of volume V . The average number of particles contained in a volume element $d\mathbf{r}$ about position \mathbf{r} with velocities \mathbf{v} in a range $d\mathbf{v}$ about \mathbf{v} at time t is given by the velocity distribution function $f(\mathbf{r}, \mathbf{v}, t)d\mathbf{r}d\mathbf{v}$. The total number of particles N in the volume V is

$$\frac{N}{V} = \int f(\mathbf{r}, \mathbf{v}, t)d\mathbf{v}. \quad (2.1)$$

In the following we will denote the particle density N/V by n . All the particles contained in a volume element $d\mathbf{r}d\mathbf{v}$ at (\mathbf{r}, \mathbf{v}) , at time t , will be contained in a volume element $d\mathbf{r}'d\mathbf{v}'$ at $(\mathbf{r} + \mathbf{v}\Delta t, \mathbf{v} + \mathbf{F}/m\Delta t, t + \Delta t)$, at time $t + \Delta t$. In the absence of collisions between the particles

$$f\left(\mathbf{r} + \mathbf{v}\Delta t, \mathbf{v} + \frac{\mathbf{F}}{m}\Delta t, t + \Delta t\right) d\mathbf{r}'d\mathbf{v}' = f(\mathbf{r}, \mathbf{v}, t)d\mathbf{r}d\mathbf{v}, \quad (2.2)$$

with \mathbf{F} the external force and m the particle's mass. It can be shown that in the absence of collisions, the volume element remains unchanged under evolution in time [29], that is $d\mathbf{r}d\mathbf{v} = d\mathbf{r}'d\mathbf{v}'$. Then equation (2.2) reduces to

$$f\left(\mathbf{r} + \mathbf{v}\Delta t, \mathbf{v} + \frac{\mathbf{F}}{m}\Delta t, t + \Delta t\right) = f(\mathbf{r}, \mathbf{v}, t). \quad (2.3)$$

In the presence of collisions equation (2.3) is

$$f\left(\mathbf{r} + \mathbf{v}\Delta t, \mathbf{v} + \frac{\mathbf{F}}{m}\Delta t, t + \Delta t\right) - f(\mathbf{r}, \mathbf{v}, t) = \left(\frac{\partial f}{\partial t}\right)_{coll} \Delta t, \quad (2.4)$$

where $(\partial f/\partial t)_{coll}$ is the collision operator, as the name implies, this term represents the collisions of one particle with another. We expand the left hand side of this equation to the first order in Δt . We obtain the equation of motion for the velocity distribution function

$$\frac{\partial f(\mathbf{r}, \mathbf{v}, t)}{\partial t} = \left(\frac{\partial}{\partial t} + \mathbf{v} \cdot \nabla_{\mathbf{r}} + \frac{\mathbf{F}}{m} \cdot \nabla_{\mathbf{v}}\right) f(\mathbf{r}, \mathbf{v}, t) = \left(\frac{\partial f}{\partial t}\right)_{coll}, \quad (2.5)$$

where

$$\nabla_{\mathbf{r}} = \left(\frac{\partial}{\partial x}, \frac{\partial}{\partial y}, \frac{\partial}{\partial z}\right), \quad \nabla_{\mathbf{v}} = \left(\frac{\partial}{\partial v_x}, \frac{\partial}{\partial v_y}, \frac{\partial}{\partial v_z}\right). \quad (2.6)$$

The derivation process of the collision operator $(\partial f / \partial t)_{coll}$ is presented in [29], where binary collisions and the assumption of molecular chaos are considered. Boltzmann's transport equation is

$$\begin{aligned} \frac{\partial f(\mathbf{r}, \mathbf{v}, t)}{\partial t} = & \left(\frac{\partial}{\partial t} + \mathbf{v} \cdot \nabla_{\mathbf{r}} + \frac{\mathbf{F}}{m} \cdot \nabla_{\mathbf{v}_1} \right) f(\mathbf{r}, \mathbf{v}_1, t) = \\ & \int d\mathbf{v}_2 \int \sigma(\Omega) d\Omega |\mathbf{v}_2 - \mathbf{v}_1| [f(\mathbf{r}, \mathbf{v}'_1, t) f(\mathbf{r}, \mathbf{v}'_2, t) - f(\mathbf{r}, \mathbf{v}_1, t) f(\mathbf{r}, \mathbf{v}_2, t)] , \end{aligned} \quad (2.7)$$

in this expression $(\mathbf{v}_1, \mathbf{v}_2)$ and $(\mathbf{v}'_1, \mathbf{v}'_2)$ are the initial and final velocities of any possible collision and $\sigma(\Omega)$ is the differential cross section of the solid angle Ω .

2.3 The equilibrium distribution function $f^{(eq)}$

The equilibrium distribution function $f^{(eq)}$ is the solution to the equation (2.7) when $\partial f(\mathbf{v}, t)/\partial t = 0$. Hence, equation (2.7) is

$$\int d\mathbf{v}_2 \int \sigma(\Omega) d\Omega |\mathbf{v}_2 - \mathbf{v}_1| \left[f^{(eq)}(\mathbf{r}, \mathbf{v}'_1, t) f^{(eq)}(\mathbf{r}, \mathbf{v}'_2, t) - f^{(eq)}(\mathbf{r}, \mathbf{v}_1, t) f^{(eq)}(\mathbf{r}, \mathbf{v}_2, t) \right] = 0. \quad (2.8)$$

A sufficient condition that satisfies the integral of the left hand side of this equation is

$$f^{(eq)}(\mathbf{v}'_1) f^{(eq)}(\mathbf{v}'_2) = f^{(eq)}(\mathbf{v}_1) f^{(eq)}(\mathbf{v}_2). \quad (2.9)$$

We take the logarithm of both sides

$$\ln f^{(eq)}(\mathbf{v}'_1) + \ln f^{(eq)}(\mathbf{v}'_2) = \ln f^{(eq)}(\mathbf{v}_1) + \ln f^{(eq)}(\mathbf{v}_2), \quad (2.10)$$

this equation has the form of a conservation law. The general solution is

$$\ln f^{(eq)}(\mathbf{v}) = \lambda_1(\mathbf{v}) + \lambda_2(\mathbf{v}) + \lambda_3(\mathbf{v}) \dots \quad (2.11)$$

where λ_1 , λ_2 and λ_3 represent the conservation of mass, momentum and energy, respectively. Therefore $\ln f^{(eq)}$ is a linear combination of \mathbf{v}^2 and the three components of the velocity \mathbf{v} plus an arbitrary constant

$$\ln f^{(eq)}(\mathbf{v}) = -A(\mathbf{v} - \mathbf{u})^2 + \ln C \quad (2.12)$$

or

$$f^{(eq)}(\mathbf{v}) = C \exp \left[-A(\mathbf{v} - \mathbf{u})^2 \right], \quad (2.13)$$

where C , A and \mathbf{u} are five arbitrary constants. Substituting $f^{(eq)}(\mathbf{v})$ into the equation (2.1), the particle density n is

$$n = C \int \exp \left[-A(\mathbf{v} - \mathbf{u})^2 \right] d\mathbf{v}, \quad (2.14)$$

with $\mathbf{u} = 0$, the above equation becomes

$$n = C \int \exp \left[-A\mathbf{v}^2 \right] d\mathbf{v}. \quad (2.15)$$

The solution of this equation is

$$n = C \left(\frac{\pi}{A} \right)^{3/2}, \quad (2.16)$$

then

$$C = n \left(\frac{A}{\pi} \right)^{3/2}. \quad (2.17)$$

The average velocity \mathbf{u} is defined by

$$\mathbf{u} = \frac{1}{n} \int \mathbf{v} f^{(eq)}(\mathbf{v}) d\mathbf{v}. \quad (2.18)$$

The average kinetic energy $\langle \epsilon \rangle$ of a particle is

$$\langle \epsilon \rangle = \frac{m}{2n} \int |\mathbf{v}^2 - \mathbf{u}^2| f^{(eq)}(\mathbf{v}) d\mathbf{v}, \quad (2.19)$$

with m the particle's mass. We assume there is energy equipartition, hence equation (2.19) is associated with the temperature T through Boltzmann's constant k by

$$\langle \epsilon \rangle = \frac{D}{2} kT, \quad (2.20)$$

with D the number of dimensions. It can be shown that the constant A is related to the average energy by [29]

$$A = \frac{m}{2kT}. \quad (2.21)$$

Substituting A in equation (2.17)

$$C = n \left(\frac{m}{2\pi kT} \right)^{3/2}. \quad (2.22)$$

Then

$$f^{(eq)}(\mathbf{v}) = n \left(\frac{m}{2\pi kT} \right)^{3/2} \exp \left[-m \frac{(\mathbf{v} - \mathbf{u})^2}{2kT} \right]. \quad (2.23)$$

This is the Maxwell-Boltzmann's distribution function which describes the probability to find a particle with velocity \mathbf{v} under equilibrium conditions,

with the particle density n , the average velocity \mathbf{u} and the temperature T given by

$$n(\mathbf{r}, t) = \int f(\mathbf{r}, \mathbf{v}, t) d\mathbf{v}, \quad (2.24a)$$

$$\mathbf{u}(\mathbf{r}, t) = \frac{1}{n} \int \mathbf{v} f(\mathbf{r}, \mathbf{v}, t) d\mathbf{v}, \quad (2.24b)$$

$$T(\mathbf{r}, t) = \frac{m}{Dkn} \int |\mathbf{v} - \mathbf{u}|^2 f(\mathbf{r}, \mathbf{v}, t) d\mathbf{v}. \quad (2.24c)$$

equation (2.23) can be written as

$$f^{(eq)}(\mathbf{v}, \mathbf{u}) = n \left(\frac{m}{2\pi kT} \right)^{3/2} \exp \left(\frac{-m\mathbf{v}^2}{2kT} \right) a(\mathbf{v}, \mathbf{u}) \quad (2.25)$$

with

$$a(\mathbf{v}, \mathbf{u}) = \exp \left(m \frac{\mathbf{v} \cdot \mathbf{u}}{kT} - m \frac{\mathbf{u}^2}{2kT} \right). \quad (2.26)$$

In the low Mach number approximation, the velocity is considered to be small. We apply a Taylor expansion of the term $a(\mathbf{v}, \mathbf{u})$ up to the second order

$$a(\mathbf{v}, \mathbf{u}) = 1 + \nabla a(0, 0) \cdot \mathbf{u} + \frac{1}{2} \mathbf{u} \cdot \mathbf{H}(0, 0) \cdot \mathbf{u}^T, \quad (2.27)$$

where

$$\nabla a(0, 0) \cdot \mathbf{u} = m \frac{\mathbf{v} \cdot \mathbf{u}}{kT}, \quad (2.28)$$

$(\mathbf{u})^T$ is the transpose of \mathbf{u} and $\mathbf{H}(0, 0)$ the Hessian. The low Mach number approximation of the equilibrium distribution function $f^{(eq)}(\mathbf{v})$ is

$$f^{(eq)}(\mathbf{v}) = n \left(\frac{m}{2\pi kT} \right)^{D/2} \exp \left(-m \frac{\mathbf{v}^2}{2kT} \right) \left[1 + \frac{m}{kT} (\mathbf{v} \cdot \mathbf{u}) + \left(\frac{m}{kT} \right)^2 (\mathbf{v} \cdot \mathbf{u})^2 - \frac{m}{kT} \mathbf{u}^2 \right]. \quad (2.29)$$

2.4 Discretization of Boltzmann's transport equation

In the Bhatnagar, Gross and Krook (BGK) approximation [13, 14], the collision operator given by the right hand side of the equation (2.7) is replaced by a relaxation to the local equilibrium term of the form

$$\left(\frac{\partial f}{\partial t}\right)_{coll} = \frac{1}{\tau} \left[f^{(eq)}(\mathbf{r}, \mathbf{v}, t) - f(\mathbf{r}, \mathbf{v}, t) \right], \quad (2.30)$$

where $f(\mathbf{r}, \mathbf{v}, t)$ is the velocity distribution function, \mathbf{v} is the microscopic velocity, τ is the relaxation time and $f^{(eq)}(\mathbf{r}, \mathbf{v}, t)$ is Maxwell Boltzmann's distribution function. Substituting the relaxation to the local equilibrium term into the equation (2.5) we obtain

$$f\left(\mathbf{r} + \mathbf{v}\Delta t, \mathbf{v} + \frac{\mathbf{F}}{m}\Delta t, t + \Delta t\right) - f(\mathbf{r}, \mathbf{v}, t) = \frac{\Delta t}{\tau} \left[f(\mathbf{r}, \mathbf{v}, t) - f^{(eq)}(\mathbf{r}, \mathbf{v}, t) \right]. \quad (2.31)$$

To discretize the BTE in the BGK approximation, the above equation can be rewritten as

$$\frac{df}{dt} + \frac{1}{\tau}f = \frac{1}{\tau}f^{(eq)}. \quad (2.32)$$

This equation has the form of a linear first order differential equation that can be solved using the technique of an integrating factor $\mu = e^{t/\tau}$. We multiply equation (2.32) by μ

$$\frac{d}{dt} \left(f e^{t/\tau} \right) = \frac{1}{\tau} f^{(eq)} e^{t/\tau}. \quad (2.33)$$

Integrating both sides we obtain

$$f\left(\mathbf{r} + \mathbf{v}\Delta t, \mathbf{v} + \frac{\mathbf{F}}{m}\Delta t, t + \Delta t\right) = \frac{1}{\tau} e^{-\Delta t/\tau} \int_0^{\Delta t} e^{t/\tau} f^{(eq)}\left(\mathbf{r} + \mathbf{v}\Delta t, \mathbf{v} + \frac{\mathbf{F}}{m}\Delta t, t + \Delta t\right) dt + e^{(-\Delta t/\tau)} f(\mathbf{r}, \mathbf{v}, t). \quad (2.34)$$

To linearize $f^{(eq)}$, we assume that Δt is small

$$f^{(eq)}\left(\mathbf{r} + \mathbf{v}\Delta t, \mathbf{v} + \frac{\mathbf{F}}{m}\Delta t, t + \Delta t\right) = \left(1 - \frac{t}{\Delta t}\right) f(\mathbf{r}, \mathbf{v}, t) + \frac{t}{\Delta t} f^{(eq)}\left(\mathbf{r} + \mathbf{v}\Delta t, \mathbf{v} + \frac{\mathbf{F}}{m}\Delta t, t + \Delta t\right). \quad (2.35)$$

Substituting the above expression into the equation (2.34) and integrating the resulting equation, we obtain

$$\begin{aligned}
 f\left(\mathbf{r} + \mathbf{v}\Delta t, \mathbf{v} + \frac{\mathbf{F}}{m}\Delta t, t + \Delta t\right) - f(\mathbf{r}, \mathbf{v}, t) = \\
 \left(e^{-\Delta t/\tau} - 1\right) \left(f(\mathbf{r}, \mathbf{v}, t) - f^{(eq)}(\mathbf{r}, \mathbf{v}, t)\right) + \\
 \left(1 + \frac{\tau}{\Delta t}(e^{-\Delta t/\tau} - 1)\right) f^{(eq)}\left(\mathbf{r} + \mathbf{v}\Delta t, \mathbf{v} + \frac{\mathbf{F}}{m}\Delta t, t + \Delta t\right).
 \end{aligned} \tag{2.36}$$

We expand $e^{-\Delta t/\tau}$ to the first order Taylor series in Δt and neglect the terms of order $\mathcal{O}(\Delta t^2)$, equation (2.36) leads to

$$f\left(\mathbf{r} + \mathbf{v}\Delta t, \mathbf{v} + \frac{\mathbf{F}}{m}\Delta t, t + \Delta t\right) - f(\mathbf{r}, \mathbf{v}, t) = -\frac{\Delta t}{\tau} \left[f(\mathbf{r}, \mathbf{v}, t) - f^{(eq)}(\mathbf{r}, \mathbf{v}, t)\right]. \tag{2.37}$$

This equation is the discretization of the BTE in the BGK approximation.

2.5 The lattice Boltzmann equation method in the D2Q9 model

The Chapman-Enskog hypothesis states that the moments of equations (2.24) can be evaluated with $f^{(eq)}$

$$I_{m,n} = \int \psi_{m,n}(\mathbf{v}) f(\mathbf{r}, \mathbf{v}) d\mathbf{v} = \int \psi_{m,n}(\mathbf{v}) f^{(eq)}(\mathbf{r}, \mathbf{v}) d\mathbf{v}, \quad (2.38)$$

where $\psi_{m,n}$ is a polynomial of \mathbf{v} and the m th and n th order. The integral of equation (2.38) has the form

$$\int \psi(\zeta) \exp^{-\zeta^2} d\zeta, \quad (2.39)$$

which can be calculated with Gaussian quadrature [30]. The LBEM in a two dimensional lattice with nine velocities is known as the D2Q9 model. In this model the polynomial ψ is

$$\psi_{m,n}(\mathbf{v}) = v_x^m v_y^n \quad (2.40)$$

where v_x^m and v_y^n are the x and y components of \mathbf{v} . Substituting $\psi_{m,n}(\mathbf{v})$ and $f^{(eq)}$ into the equation (2.38)

$$\begin{aligned} I_{m,n} = \int \psi_{m,n}(\mathbf{v}) f^{(eq)} d\mathbf{v} &= \frac{\rho}{2\pi kT} \left[\int v_x^m v_y^n \exp\left(\frac{-\mathbf{v}^2}{2kT}\right) \left(1 - \frac{\mathbf{u}^2}{2kT}\right) dv_x dv_y \right. \\ &\quad + \int v_x^m v_y^n \exp\left(\frac{-\mathbf{v}^2}{2kT}\right) \left(\frac{\mathbf{v} \cdot \mathbf{u}}{2kT}\right) dv_x dv_y \\ &\quad \left. + \int v_x^m v_y^n \exp\left(\frac{-\mathbf{v}^2}{2kT}\right) \frac{1}{2} \left(\frac{\mathbf{v} \cdot \mathbf{u}}{kT}\right)^2 dv_x dv_y \right]. \end{aligned} \quad (2.41)$$

We denote the above equation as

$$I = A + B + C, \quad (2.42)$$

with

$$A = \frac{\rho}{\pi} \left(\sqrt{2kT}\right)^{m+n} \left(1 - \frac{\mathbf{u}}{2kT} I_m I_n\right), \quad (2.43)$$

$$B = \frac{\rho}{\pi} \left(\sqrt{2kT}\right)^{m+n} \left(\frac{2u_x I_{m+1} I_n + 2u_y I_m I_{n+1}}{\sqrt{2kT}}\right) \quad (2.44)$$

and

$$C = \frac{\rho}{\pi} \left(\sqrt{2kT} \right)^{m+n} \left(\frac{u_x^2 I_{m+2} I_n + 2u_x u_y I_{m+1} I_{n+1} + u_y^2 I_m I_{n+2}}{kT} \right), \quad (2.45)$$

where

$$I_m = \int_{-\infty}^{\infty} \exp^{-\zeta^2} \zeta^m d\zeta, \quad \zeta = \mathbf{v} / \sqrt{2kT}, \quad (2.46)$$

is the m th order moment of the weight function $\exp^{-\zeta^2}$. This equation can be evaluated with the third order Hermite formula given by

$$I_m = \sum_{j=1}^3 \omega_j \zeta_j^m, \quad (2.47)$$

where ζ_k are the set of k discrete velocities or abscissas and ω_k are the weight coefficients of the quadrature. Substituting equation (2.47) into equation (2.43)

$$\begin{aligned} A &= \frac{\rho}{\pi} \left(1 - \frac{\mathbf{u}^2}{2kT} \right) \sum_{i=1}^3 \omega_i (2kT)^{m/2} \zeta_i^m \sum_{j=1}^3 \omega_j (2kT)^{n/2} \zeta_j^n \\ &= \frac{\rho}{\pi} \sum_{i,j} \omega_i \omega_j \psi_{m,n}(\mathbf{v}_{i,j}) \left(1 - \frac{u^2}{2kT} \right), \end{aligned} \quad (2.48)$$

with

$$\mathbf{v}_{i,j} = (\mathbf{v}_i, \mathbf{v}_j) = \sqrt{2kT}(\zeta_i, \zeta_j), \quad \psi_{m,n}(\mathbf{v}_{i,j}) = \zeta_i^m \zeta_j^n, \quad (2.49)$$

From equations (2.44) and (2.45)

$$\begin{aligned} B &= \frac{\rho}{\pi kT} \left(u_x \sum_{i,j=1}^2 \omega_i \omega_j \psi_{m,n}(\mathbf{v}_{i,j}) v_i + u_y \sum_{i,j=1}^3 \omega_i \omega_j \psi_{m,n}(\mathbf{v}_{i,j}) v_j \right), \\ B &= \frac{\rho}{\pi} \sum_{i,j} \omega_i \omega_j \psi_{m,n}(\mathbf{v}_{i,j}) \left(\frac{\mathbf{v}_i \mathbf{v}_j \cdot \mathbf{u}}{kT} \right), \end{aligned} \quad (2.50)$$

and

$$\begin{aligned} C &= \frac{\rho}{\pi} \omega_i \omega_j \psi_{m,n}(\mathbf{v}_{i,j}) \left(\frac{u_x^2 v_i^2 + 2u_x u_y v_i v_j + u_y^2 v_j^2}{2(kT^2)} \right), \\ C &= \frac{\rho}{\pi} \sum_{i,j=1}^3 \omega_i \omega_j \psi_{m,n}(\mathbf{v}_{i,j}) \left[\frac{((\mathbf{v}_i, \mathbf{v}_j) \cdot \mathbf{u})^2}{2(kT)^2} \right]. \end{aligned} \quad (2.51)$$

The integral of equation (2.47) becomes

$$I_{m,n} = \frac{\rho}{\pi} \sum_{i,j=1}^3 \omega_i \omega_j \psi_{m,n}(\mathbf{v}_{i,j}) \left[\left(1 - \frac{\mathbf{u}^2}{2kT} \right) + \left(\frac{\mathbf{v}_{i,j} \cdot \mathbf{u}}{kT} \right) + \frac{1}{2} \left(\frac{\mathbf{v}_{i,j} \cdot \mathbf{u}}{kT} \right)^2 \right] \quad (2.52)$$

From the above equation we identify the equilibrium distribution function

$$f_{i,j}^{(eq)} = \frac{\omega_i \omega_j n}{\pi} \left[\left(1 - \frac{\mathbf{u}^2}{2kT} \right) + \left(\frac{\mathbf{v}_{i,j} \cdot \mathbf{u}}{kT} \right) + \frac{1}{2} \left(\frac{\mathbf{v}_{i,j} \cdot \mathbf{u}}{kT} \right)^2 \right]. \quad (2.53)$$

With equation (2.47) we rewrite equation (2.52) as follows

$$I_{m,n} = \sum_{i,j} \psi_{m,n}(\mathbf{v}_i, \mathbf{v}_j) f_{i,j}^{(eq)}(\mathbf{r}, \mathbf{v}). \quad (2.54)$$

To obtain the weight coefficients $\omega_i \omega_j$, we use the Hermite polynomial H_n defined by

$$H_n(\zeta) = (-1)^n \exp^{\zeta^2} \frac{d^n}{d\zeta^n} \left[\exp(-\zeta^2) \right]. \quad (2.55)$$

The third order Hermite formula is

$$H_3(\zeta) = (-1)^3 \exp^{\zeta^2} \frac{d^3}{d\zeta^3} \left[\exp(-\zeta^2) \right] = 8\zeta^3 - 12\zeta. \quad (2.56)$$

The three abscissas of the quadrature are

$$\zeta_1 = -\sqrt{3/2}, \quad \zeta_2 = 0, \quad \zeta_3 = \sqrt{3/2}. \quad (2.57)$$

The weight coefficients given by the Hermite formula are

$$\omega_k = \frac{2^{n+1} n! \sqrt{\pi}}{H'_n(\zeta_j)^2}, \quad (2.58)$$

with H'_n the first derivative of the Hermite polynomial of order n . The first derivative of equation (2.56) is

$$H'_3(\zeta) = 24\zeta^2 - 12. \quad (2.59)$$

The roots of this equation are

$$H'_3(\zeta_1) = 24, \quad H'_3(\zeta_2) = -12, \quad H'_3(\zeta_3) = 24, \quad (2.60)$$

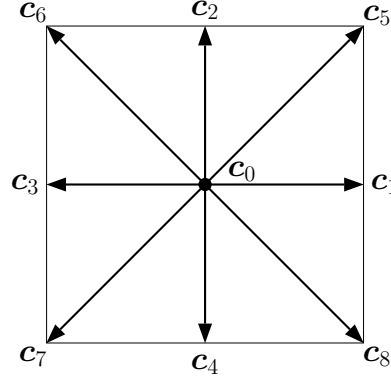


Figure 2.1: Schematic representation of the discrete velocity vectors \mathbf{c}_k for the $D2Q9$ model.

and the weight coefficients

$$\omega_1 = \sqrt{\pi}/6, \quad \omega_2 = 2\sqrt{\pi}/3, \quad \omega_3 = \sqrt{\pi}/6. \quad (2.61)$$

In figure 2.1 we show the nine different velocity directions \mathbf{c}_k of the $D2Q9$ model. The velocities \mathbf{c}_k are

$$\mathbf{c}_k = \begin{cases} (0,0), & k = 0 \\ c(\cos(\phi_k), \sin(\phi_k)), & k = 1, \dots, 4 \\ c\sqrt{2}(\cos(\psi_k), \sin(\psi_k)), & k = 5, \dots, 8. \end{cases} \quad (2.62)$$

with $k = 0, \dots, 8$, $\phi_k = \pi(k - 1/2)$, $\psi_k = \pi(k - 9/2)$, and the speed of the lattice $c = \Delta x / \Delta t = 1$. The discrete velocity $\mathbf{v}_{i,j}$ defined by equation (2.49) for $i, j = (1, 1)$ is

$$\mathbf{v}_{1,1} = \sqrt{2kT}(\zeta_1, \zeta_1) = \sqrt{2kT}\sqrt{3/2}(-1, -1), \quad (2.63)$$

$$\mathbf{v}_{1,1} = \sqrt{3kT}(-1, -1) = \sqrt{3kT}\mathbf{c}_7. \quad (2.64)$$

The weight coefficient in this case is

$$\omega_1\omega_1 = \frac{\sqrt{\pi}}{6} \frac{\sqrt{\pi}}{6} = \frac{\pi}{36}. \quad (2.65)$$

The substitution of the rest of the values of (i, j) for the set of discrete velocities vectors $\mathbf{v}_{i,j}$ and weight coefficients ω_k are shown in table 2.1.

i	j	$\mathbf{v}_{i,j}/\sqrt{3kT}$	$\omega_i\omega_j/\pi = \omega_k$	\mathbf{c}_k
1	1	(-1,-1)	1/36	\mathbf{c}_7
1	2	(-1,0)	1/9	\mathbf{c}_3
1	3	(-1,1)	1/36	\mathbf{c}_6
2	1	(0,-1)	1/9	\mathbf{c}_4
2	2	(0,0)	4/9	\mathbf{c}_0
2	3	(0,1)	1/9	\mathbf{c}_2
3	1	(1,-1)	1/36	\mathbf{c}_8
3	2	(1,0)	1/9	\mathbf{c}_1
3	3	(1,1)	1/36	\mathbf{c}_5

Table 2.1: The set of discrete velocities vectors $\mathbf{v}_{i,j}$ and weight coefficients ω_k of the D2Q9 model.

From equation (2.53) in terms of \mathbf{c}_k and ω_k , we obtain the equilibrium distribution function for the D2Q9 model given by

$$f_k^{(eq)}(\mathbf{r}) = \omega_k n \left[1 + \frac{(\mathbf{c}_k \cdot \mathbf{u})}{c_s^2} + \frac{(\mathbf{c}_k \cdot \mathbf{u})^2}{2c_s^4} - \frac{\mathbf{u}^2}{2c_s^2} \right], \quad (2.66)$$

with the substitution $kT = c_s^2 = c^2/3$, with c_s the speed of sound [30]. The particle density n and the velocity \mathbf{u} are given by

$$n(\mathbf{r}, t) = \sum_{k=0}^8 f_k(\mathbf{r}, t) \quad \mathbf{u}(\mathbf{r}, t) = \sum_{k=0}^8 \mathbf{c}_k f_k(\mathbf{r}, t). \quad (2.67)$$

The velocity distribution function in the BGK approximation is

$$f_k(\mathbf{r} + \mathbf{c}_k \Delta t, t + \Delta t) - f_k(\mathbf{r}, t) = -\frac{\Delta t}{\tau} \left[f_k(\mathbf{r}, t) - f_k^{(eq)}(\mathbf{r}, t) \right] + F_k, \quad (2.68)$$

In this equation $f_k(\mathbf{r}, t)$ is the probability of a particle being at position \mathbf{r} at time t with velocity \mathbf{c}_k , $f_k^{(eq)}$ is the local equilibrium distribution function given by the equation (2.66). In section 2.7, we show that the relaxation time τ is related to the kinematic viscosity ν by

$$\nu = c_s^2 (\tau - \tau_0), \quad (2.69)$$

with $\tau_0 = 1/2$. The term F_k represents a body force like gravitation, pressure difference or electromagnetic forces in a dimensionless form. The general form of F_k is

$$F_k = 3\omega_k (c_{kx}G_x + c_{ky}G_y) , \quad (2.70)$$

where c_{kx} and c_{ky} are the horizontal and vertical component of \mathbf{c}_k , respectively. In chapter 4, we simulate a pressure gradient in the x direction, in this case equation (2.70) is

$$F_x = 3\omega_k c_{kx} G_x, \quad (2.71)$$

with $G_x = \hat{P}'$, given by

$$\hat{P}' = \frac{8\nu^2 \rho Re}{L_y^3}. \quad (2.72)$$

We will further discuss the body force \hat{P}' in chapter 4, section 4.2.

2.6 The temperature field

The temperature T is defined by [7]

$$T(\mathbf{r}, t) = \sum_{i=0}^8 T_k(\mathbf{r}, t) \quad (2.73)$$

with $k = 0, \dots, 8$ and T_k is the temperature distribution function in the BGK approximation at position \mathbf{r} with velocity \mathbf{c}_k and time t that obeys the transport equation

$$T_k(\mathbf{r} + \Delta t \mathbf{c}_k, t + \Delta t) - T_k(\mathbf{r}, t) = -\frac{\Delta t}{\tau_T} \left[T_k(\mathbf{r}, t) - T_k^{(eq)}(\mathbf{r}, t) \right], \quad (2.74)$$

where τ_T is the relaxation time for the temperature field related to the thermal diffusivity α [7] by

$$\alpha = c_s^2 (\tau_T - \tau_0), \quad (2.75)$$

with $\tau_0 = 0.5$, $c_s = 1/\sqrt{3}$ the speed of sound, $\alpha > 0$ and $\tau_T > 0.5$.

The equilibrium distribution function for the temperature field $T_k^{(eq)}$ [8] is

$$T_k^{(eq)}(\mathbf{r}, t) = \omega_k T_k \left[1 + \frac{\mathbf{c}_k \cdot \mathbf{u}}{c_s^2} \right]. \quad (2.76)$$

The weight coefficients ω_k and the velocities \mathbf{c}_k are shown in table 2.1.

Natural convection in LBEM is simulated by adding a body force F_k with the Boussinesq approximation to the buoyancy force to the left hand side of equation (2.68),

$$F_k = -3\omega_k c_{ky} G_y, \quad (2.77)$$

with G_y

$$G_y = g\beta(T - T_0). \quad (2.78)$$

In these expressions c_{ky} is the vertical component of \mathbf{c}_k , g is the acceleration due to gravity in the lattice, β is the thermal expansion coefficient and T_0 a reference temperature. We will further discuss the Boussinesq approximation in section 4.3.

2.7 The Chapman-Enskog expansion

The macroscopic hydrodynamic equations can be derived through the Chapman and Enskog procedure [15, 7], which is a multiscaling expansion technique for solving Boltzmann's Equation. To see this, we first use a Taylor expansion in time and space of the left hand side of equation (2.4)

$$f_k(\mathbf{r} + \mathbf{c}_k \Delta t, t + \Delta t) = f_k(\mathbf{r}, t) + \Delta t (\mathbf{c}_k \cdot \nabla) f_k(\mathbf{r}, t) + \frac{\Delta t^2}{2} \left(\frac{\partial}{\partial t} + \mathbf{c}_k \cdot \nabla \right)^2 f_k(\mathbf{r}, t). \quad (2.79)$$

Substituting equation (2.79) in equation (2.68)

$$f_k(\mathbf{r}, t) + \Delta t (\mathbf{c}_k \cdot \nabla) f_k(\mathbf{r}, t) + \frac{\Delta t^2}{2} \left(\frac{\partial}{\partial t} + \mathbf{c}_k \cdot \nabla \right)^2 f_k(\mathbf{r}, t) = \frac{\Delta t}{\tau} \left[f_k(\mathbf{r}, t) - f_k^{(eq)}(\mathbf{r}, t) \right]. \quad (2.80)$$

We expand the particle distribution function $f_k(\mathbf{r}, t)$ about the local equilibrium distribution function $f_k^{(eq)}$

$$f_k(\mathbf{r}, t) = f_k^{(eq)} + \epsilon f_k^{(neq)}, \quad (2.81)$$

where $f_k^{(eq)} = f_k^{(0)}$, the equilibrium distribution function, $f_k^{(neq)} = f_k^{(1)}(\mathbf{r}, t) + \epsilon f_k^{(2)}(\mathbf{r}, t) + \dots$ is the non equilibrium distribution function and ϵ is a small parameter proportional to the Knudsen number, given by the ratio between the mean free path and the representative flow length scale. We introduce two macroscopic time scales and a length scale

$$\left[\frac{\partial}{\partial t} = \epsilon \frac{\partial}{\partial t_1} + \epsilon^2 \frac{\partial}{\partial t_2}, \quad \nabla = \epsilon \nabla \right]. \quad (2.82)$$

Inserting the expressions (2.81) and (2.82) in the equation (2.80),

$$\begin{aligned} & \left(\epsilon \frac{\partial}{\partial t_1} + \epsilon^2 \frac{\partial}{\partial t_2} \right) \left(f_k^{(0)} + \epsilon f_k^{(1)} + \epsilon^2 f_k^{(2)} \right) + (\mathbf{c}_k \cdot \epsilon \nabla) \left[f_k^{(0)} + \epsilon f_k^{(1)} + \epsilon^2 f_k^{(2)} \right] + \\ & \frac{1}{2} \left[\left(\epsilon \frac{\partial}{\partial t_1} + \epsilon^2 \frac{\partial}{\partial t_2} \right)^2 + 2 \left(\epsilon \frac{\partial}{\partial t_1} + \epsilon^2 \frac{\partial}{\partial t_2} \right) (\mathbf{c}_k \cdot \epsilon \nabla) + (\mathbf{c}_k \cdot \epsilon \nabla)^2 \right] = \\ & \frac{1}{\tau} \left[f_k^{(0)} + \epsilon f_k^{(1)} + \epsilon^2 f_k^{(2)} - f_k^{(eq)} \right]. \end{aligned} \quad (2.83)$$

Collecting the terms of first order ϵ^1

$$\frac{\partial}{\partial t_1} f_k^{(eq)} + (\mathbf{c}_k \cdot \epsilon \nabla) f_k^{(eq)} = -\frac{f_k^{(1)}}{\tau}, \quad (2.84)$$

and second order ϵ^2

$$\begin{aligned} \frac{\partial}{\partial t_1} f_k^{(1)} + \frac{\partial}{\partial t_2} f_k^{(eq)} + (\mathbf{c}_k \cdot \epsilon \nabla) f_k^{(1)} + \frac{1}{2} \frac{\partial^2}{\partial t_1^2} f_k^{(eq)} + \\ \frac{\partial}{\partial t_1} (\mathbf{c}_k \cdot \epsilon \nabla) f_k^{(eq)} + \frac{1}{2} \mathbf{c}_k \mathbf{c}_k \cdot \nabla^2 f_k^{(eq)} = \frac{1}{\tau} f_k^{(eq)}. \end{aligned} \quad (2.85)$$

We can rewrite equation (2.85) by using the equation (2.84)

$$\frac{\partial}{\partial t_2} f_k^{(eq)} + \left(1 - \frac{1}{2\tau}\right) \left[\frac{\partial}{\partial t_1} f_k^{(1)} + (\mathbf{c}_k \cdot \nabla) f_k^{(1)} \right] = -\frac{f_k^{(2)}}{\tau}. \quad (2.86)$$

From equation (2.84) and (2.86) we can obtain the macroscopic mass and momentum equations

$$\frac{\partial \rho}{\partial t} + \nabla \cdot \rho \mathbf{u} = 0, \quad (2.87)$$

$$\frac{\partial \rho \mathbf{u}}{\partial t} + \nabla \cdot \Pi = 0, \quad (2.88)$$

where Π is the momentum flux tensor given by

$$\Pi_{\alpha\beta} = \sum_k \mathbf{c}_{k\alpha} \mathbf{c}_{k\beta} \left[f_k^{(eq)} + \left(1 - \frac{1}{2\tau}\right) f_k^{(1)} \right], \quad (2.89)$$

with $\mathbf{c}_{k\alpha}$ and $\mathbf{c}_{k\beta}$ are the components of the velocity vector \mathbf{c}_k in the α and β coordinate directions.

The momentum flux tensor Π can be specified by the lattice geometry. As we mentioned in the previous section, we consider a two dimensional square lattice with nine velocities (the $D2Q9$ model), in this case, the term $f_k^{(eq)}$ is given by equation (2.66). We substitute $f_k^{(eq)}$ into the equation (2.89) and we obtain

$$\begin{aligned} \Pi_{\alpha}^{(0)} &= \sum_k \mathbf{c}_{k\alpha} \mathbf{c}_{k\beta} f_k^{(eq)} = p \delta_{\alpha\beta} + \rho u_{\alpha} u_{\beta}, \\ \Pi_{\alpha}^{(1)} &= \left(1 - \frac{1}{2\tau}\right) \sum_k \mathbf{c}_{k\alpha} \mathbf{c}_{k\beta} f_k^{(1)} = \nu (\nabla_{\alpha} (\rho \mathbf{u}_{\beta}) + \nabla_{\beta} (\rho \mathbf{u}_{\alpha})), \end{aligned} \quad (2.90)$$

with the pressure $p = c_s^2 \rho$, $c_s = 1/\sqrt{3}$ the sound speed [31], and the kinematic viscosity $\nu = c_s^2(\tau - \tau_0)$, with $\tau_0 = 1/2$.

The momentum equation is

$$\rho \left(\frac{\partial \mathbf{u}_\alpha}{\partial t} + \nabla_\beta \cdot \mathbf{u}_\alpha \mathbf{u}_\beta \right) = -\nabla_\alpha p + \nu \nabla_\beta \cdot (\nabla_\alpha \rho \mathbf{u}_\beta + \nabla_\beta \rho \mathbf{u}_\alpha). \quad (2.91)$$

We can follow the same procedure to obtain the energy equation [7, 8, 9] determined by

$$\frac{\partial T}{\partial t} + \nabla \cdot (\mathbf{u} T) = \alpha \nabla^2 T, \quad (2.92)$$

with α the thermal diffusivity.

2.8 Conclusions

In this chapter, we discussed Boltzmann's transport equation (BTE). The stationary solution of the BTE is given by the Maxwell distribution function $f^{(eq)}$, this equation describes the probability to find a particle with velocity \mathbf{v} under equilibrium conditions. We discussed the low Mach number approximation up to the second order. Bhatnagar, Groos and Krook (BGK) proposed an approximation in which the collision integral is replaced by a relaxation to the local equilibrium term, this expresses that collisions relax the distribution function to its local equilibrium value. We obtained the hydrodynamic moments of the equilibrium distribution function $f^{(eq)}$ for the $D2Q9$ model, which is a nine velocity model in a two dimensional lattice. We discussed the discretization of the phase space in the $D2Q9$ model. We presented the lattice Boltzmann equation method for the velocity and the temperature fields. We showed that the Navier-Stokes equations can be recovered by performing the Chapman and Enskog expansion.

Chapter 3

Heat transfer in solids using the lattice Boltzmann equation method

3.1 Introduction

To test the LBEM with the temperature distribution function given by equation (2.74) in the $D2Q9$ model, we study two different problems of heat conduction in solids and compare our results with theoretical solutions.

In section 3.2, we study the heat conduction in a two dimensional solid that is heated from below. We calculate the heat flux in the vertical direction as a function of time. We use Fourier's Law to find a relation between the relaxation time for the temperature field and the thermal conductivity. We study the temperature as a function of time. We compare the results with the numerical solution of the heat equation via Fourier series and calculate the average percentual error.

In section 3.3, we study the heat transfer in a bidimensional block made of two solids, one on the top of the other with different thermal diffusivities. We study the temperature variation and compare the results with the analytic solution in a steady state.

3.2 Heat flux, thermal conductivity and thermal diffusivity

In this section, we study the heat conduction in a plane wall that is heated from below at a constant temperature T_H . The top of the wall is maintained at a constant temperature T_C . The aspect ratio of the cavity is $L_y/L_x = 1/2$. The periodic boundary conditions are used in the x direction. The top and bottom walls have Dirichlet boundary conditions [32]. We find a relation between the relaxation time for the temperature field and the thermal conductivity. We compare our results with the numerical solution of the heat equation via Fourier series.

The heat flux \mathbf{q}' is defined as the heat transfer rate per unit area and is described by Fourier's law

$$\mathbf{q} = -k'\nabla T', \quad (3.1)$$

where the negative sign shows that the heat flux goes from the higher temperature to the lower temperature, k is the thermal conductivity which is a property of the material and $\nabla T'$ is the temperature gradient given by

$$\nabla T' = \left(\frac{\partial T'}{\partial x'}, \frac{\partial T'}{\partial y'} \right). \quad (3.2)$$

Note that we denote the dimensional parameters by the superindex $'$.

In the lattice Boltzmann equation method, the heat flux is defined as [6]

$$\mathbf{q} = \sum_k (\mathbf{c}_k - \mathbf{u}) T_k(\mathbf{r}, t). \quad (3.3)$$

In the case of heat conduction in a solid $\mathbf{u} = 0$. Then equation (3.3) becomes

$$\mathbf{q} = \sum_k \mathbf{c}_k T_k(\mathbf{r}, t). \quad (3.4)$$

The general form of the heat equation [33] is

$$\frac{\partial}{\partial x'} \left(k' \frac{\partial T'}{\partial x'} \right) + \frac{\partial}{\partial y'} \left(k' \frac{\partial T'}{\partial y'} \right) + \frac{\partial}{\partial z'} \left(k' \frac{\partial T'}{\partial z'} \right) + \dot{q} = \rho' c'_p \frac{\partial T'}{\partial t'}, \quad (3.5)$$

with ρ the density and c_p the specific heat capacity at constant pressure.

In the case of a plane wall that is heated from below, the temperature is a function of the y coordinate and heat is transferred only in this direction. We assume that the thermal conductivity is constant and there is no internal generation, then equation (3.5) reduces to

$$\alpha' \frac{\partial^2 T'}{\partial y'^2} = \frac{\partial T'}{\partial t'}, \quad (3.6)$$

with the thermal diffusivity $\alpha' = k' / \rho' c'_p$ measures the rate of heat transfer through a material. The nondimensional quantities are defined by

$$\mathbf{r} = \frac{\mathbf{r}'}{L_y}, \quad t = \frac{\alpha}{L_y^2} t', \quad T = \frac{T' - T'_C}{\Delta T'}, \quad (3.7)$$

with L_y the characteristic length, L_y^2 / α the characteristic time and $\Delta T' = T'_H - T'_C$ the characteristic temperature, note that $0 \leq T \leq 1$. The initial temperature inside the plane wall is T_C .

The boundary conditions are

$$T(0) = T_H, \quad T(L_y) = T_C. \quad (3.8)$$

The solution of equation (3.6) in the steady state is

$$T^{(s)} = (T_C - T_H) y + T_H. \quad (3.9)$$

The time dependent solution of equation (3.6) using Fourier series is

$$T(y, t) = T^{(s)} + \sum_{n=1}^{\infty} C_n \sin(n\pi y) \exp\left(-n^2 \pi^2 t L_y\right), \quad (3.10)$$

with the Fourier coefficients

$$C_n = \frac{2(T_C - T_H)}{n\pi}. \quad (3.11)$$

In figure 3.1, we show the heat flux in the vertical direction q_y calculated with equation (3.4) as a function of time t for different bottom wall temperatures T_H .

From Fourier's law, we find a relation between the relaxation time for the temperature field τ_T and the thermal conductivity k . In figure 3.2(a),

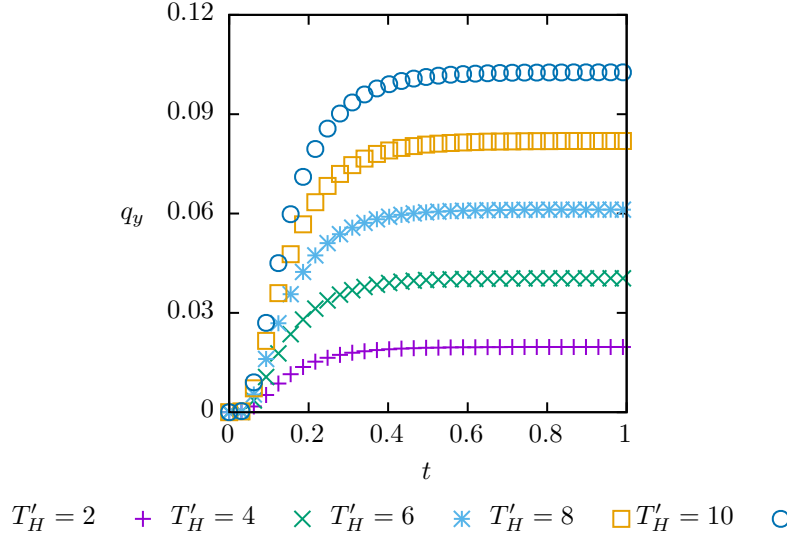


Figure 3.1: The heat flux in the vertical direction q_y as a function of time t for different bottom wall temperatures T_H . In the numerical simulations, the number of mesh sites in L_x is $N_x = 51$, the temperature $T'_C = 0.1$ and the relaxation time $\tau_T = 2$.

we show the heat flux q_y in a steady state as a function of the temperature gradient in the vertical direction $\Delta T/L_y$ for different values of τ_T . The data is fit by $q_y = -k\Delta T/L_y$ with the same values of T_H of figure 3.1. Note that the slope of every fit is the value of the thermal conductivity k . In figure 3.2(b), we show k as a function of τ_T , open squares in black. We find that the data is fit by $k(\tau_T) \approx \tau_T/3$, continuous line in black.

We study the temperature T as a function of the vertical direction y at $x = 1/2$ and different times t together with the solution of equation (3.6) given by equation (3.10) with $n = 200$, as we show in figure 3.3. The numerical simulations with the LBEM, colored squares, agree with the solution of equation (3.10) in steady and non-steady states, continuous curves and lines in black.

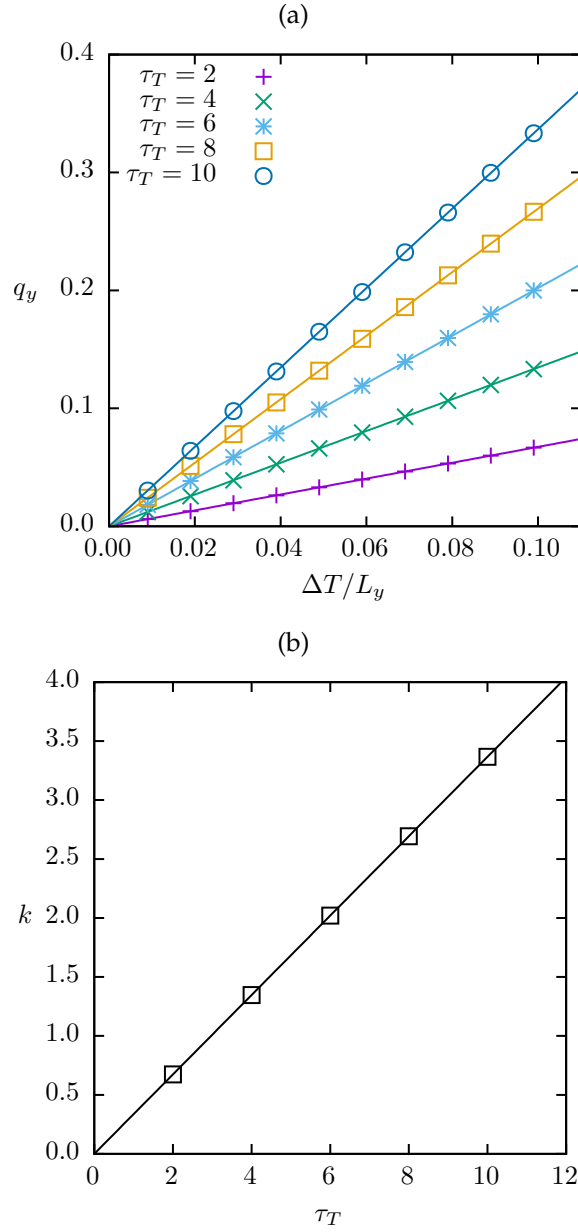


Figure 3.2: (a) The heat flux q_y in the vertical direction as a function of the temperature gradient in the vertical direction $\Delta T/L_y$ in a steady state for different relaxation times τ_T . The colored continuous lines are the fit of $q_y = k\Delta T/L_y$. (b) The thermal conductivity k as a function of the relaxation time τ_T , open squares in black. The data is fit by $k = 0.33\tau_T$, continuous line in black.

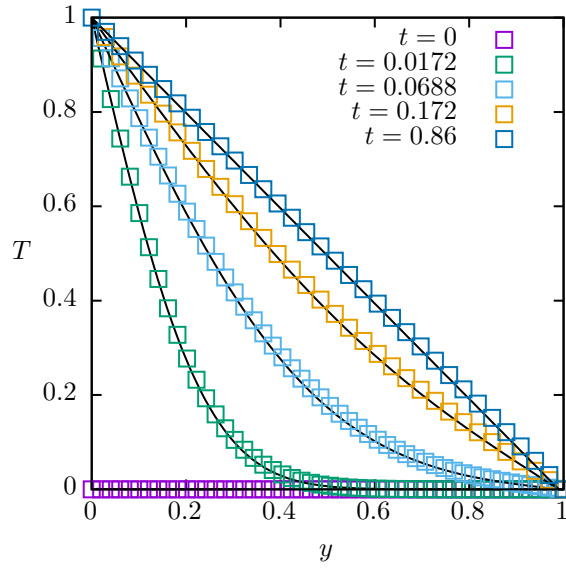


Figure 3.3: The temperature T as a function of the vertical axis y at different times t , colored squares, together with the solution of equation (3.10), shown as the continuous curves in black. The average percentual error for the temperature in a steady state is 0.00334%. In the numerical solutions, $n = 200$, $\alpha = 0.86$, $T_C = 0$, $T_H = 1$ and the number of mesh sites in L_x, L_y is $N_x = 51, N_y = 101$.

3.3 Heat conduction between two solids

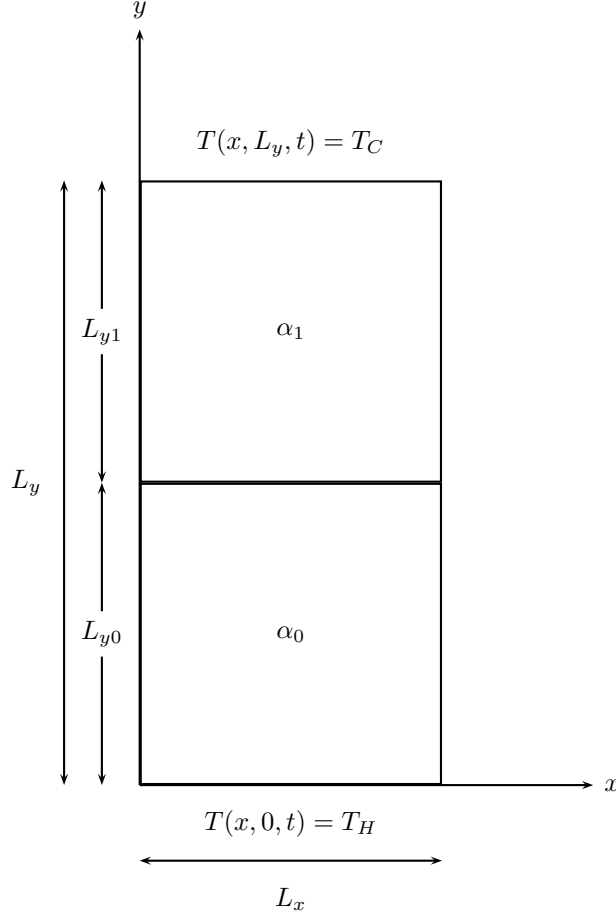


Figure 3.4: Scheme of a solid made of two different materials with different thermal diffusivities α_0 and α_1 . The length is L_x , the total height $L_y = L_{y0} + L_{y1}$ with L_{y0} and L_{y1} the heights of the bottom and the top solids respectively.

In this section, we study the heat conduction in a bidimensional solid made of two materials, one is on the top of the other with length L_x and a total height $L_y = L_{y0} + L_{y1}$, with L_{y0} and L_{y1} the heights of the bottom and the top solids respectively, this is shown in figure 3.4. The bottom and top thermal diffusivities are α_0 and α_1 with $\rho c_p = 1$ in both materials, thus

$\alpha^* = k$. The horizontal walls have the Dirichlet boundary condition [32] and the vertical walls have the periodic boundary condition. We denote the dimensional variables by the superindex $'$. The initial condition is $T'(x', y', 0) = T'_C$.

The solid is in thermal contact with heat baths at temperatures T_H and T_C in the bottom and top horizontal walls

$$T'(0, t') = T'_H, \quad T'(L_y, t') = T'_C, \quad (3.12)$$

with $T'_H > T'_C$. The boundary condition at the interface $y' = L_{y0}$ between the solids is

$$-k_0 \frac{\partial T'}{\partial y'} \Big|_{L_{y0}^-} = -k_1 \frac{\partial T'}{\partial y'} \Big|_{L_{y0}^+}. \quad (3.13)$$

The solutions in the steady state are

$$T'(L_{y0}^-) = \frac{T'_I - T'_H}{L_{y0}} y + T'_H, \quad T'(L_{y0}^+) = \frac{T'_C - T'_I}{L_{y1}} (y - L_{y0}) + T'_I, \quad (3.14)$$

with $T_I = T(y = L_{y0})$ the interface temperature in the steady state. The non-dimensional position, time and temperature are defined by

$$\mathbf{r} = \frac{\mathbf{r}'}{L_{y0} + L_{y1}}, \quad t = \frac{t'}{\left(L_{y0}^2 / \alpha_0 + L_{y1}^2 / \alpha_1 \right)}, \quad T = \frac{T' - T'_C}{\Delta T'}, \quad (3.15)$$

with $L_{y0} + L_{y1}$ the characteristic length, $1 / (L_{y0} / \alpha_0 + L_{y1} / \alpha_1)$ the characteristic time and $\Delta T' = T'_H - T'_C$ the characteristic temperature. The derivatives in equation (3.13) are taken on the left and right of $y = L_{y0}$, respectively. Thus, equation (3.13) is

$$-k_0 \frac{T_I - T_H}{L_{y0}} = -k_1 \frac{T_C - T_I}{L_{y1}}, \quad (3.16)$$

from this expression

$$T_I = \frac{k_0 L_{y1} T_H + k_1 L_{y0} T_C}{k_0 L_{y1} + k_1 L_{y0}}. \quad (3.17)$$

In figure 3.5, we show the temperature $T(L_x/2, y)$ as a function of the height y at different times t together with the interface temperature in

a steady state T_I , horizontal black line, given by equation (3.17) and the steady state temperature, two straight segments in black, given by equation (3.14). We show that our results are in good agreement with the analytic solutions in steady states of the temperature T as a function of y and the interface temperature T_I .

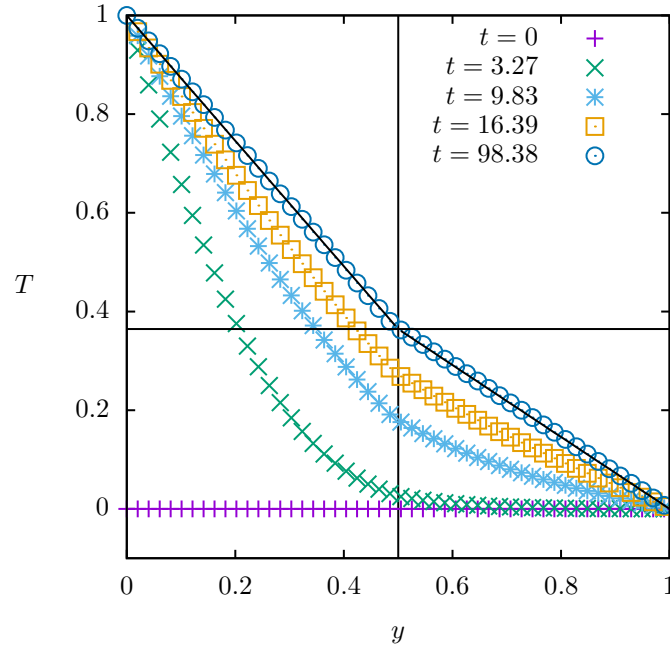


Figure 3.5: The temperature $T(L_x/2, y)$ as a function of the vertical direction y at different times t together with the interface temperature in a steady state $T_I = 0.364$, horizontal line in black, given by equation (3.17) and the steady state temperature, two straight segments in black, given by equation (3.14). The average percentual error for the temperature in a steady state is 0.65%. In the numerical simulations $T_H = 1$, $T_C = 0$, $\rho c_p = 1$, $\alpha_0 = 0.86$, $\alpha_1 = 1.5$ and the number of mesh sites in L_x, L_y with $L_y = L_{y0} + L_{y1}$ is $N_x = 51, N_y = 101$.

3.4 Conclusions

In this chapter, we studied the heat conduction in solids. In section 3.2, we presented the heat conduction in a plane wall heated from below. Our numerical results agreed with the numerical solution of the heat equation via Fourier series. The average percentage error for the temperature in a steady state was 0.00334%. We calculated the heat flux in the vertical direction q_y as a function of time t . From these results, we found a relation between the thermal conductivity and the relaxation time for the temperature field.

In section 3.3, we studied the heat transfer in a block made of two solids, one on the top of the other with different thermal diffusivities. Our results were in good agreement with the analytic solutions in steady states of the temperature as a function of the height and the interface temperature. The average percentage error for the temperature in a steady state is 0.65%.

We showed that the thermal LBEM in the $D2Q9$ model can be used to simulate problems with time dependent heat transfer.

Chapter 4

Rayleigh-Bénard-Poiseuille flow

4.1 Introduction

In this chapter, we study three different flows, Poiseuille flow, Rayleigh-Bénard convection and Rayleigh-Bénard-Poiseuille (RBP) flow with the lattice Boltzmann equation method in the $D2Q9$ model. In the LBEM for flows with heat transfer, we use two coupled distribution functions, one for the particles and the other one for temperature. These distribution functions evolve according to equations (2.68) and (2.74), respectively. To simplify the geometry of the problems, we assume that in the cavity shown in figure 4.1, the width L_z is much larger than the length L_x and the height L_y , thus all the dependent variables are independent of L_z . Then, we consider a two dimensional cavity of length L_x and height L_y with a pressure gradient in the x direction in Poiseuille flow and a temperature difference in the y direction in Rayleigh-Bénard convection. The Rayleigh-Bénard-Poiseuille flow occurs in the presence of a pressure gradient and a temperature difference.

We use Poiseuille flow and Rayleigh-Bénard convection as a benchmark tests. In section 4.2, we study Poiseuille flow. We compare our results with the analytic solution in steady and non steady states for different Reynolds numbers. We show that the average percentual error for the steady state solutions is less than 4%. In section 4.3, we study the Rayleigh-Bénard

convection in which the bottom and top walls are in thermal contact with heat baths at temperatures T_H and T_C , respectively, with $T_H > T_C$. We study the maximum vertical velocity to find the value of the relaxation time in which the transition from a conductive state to a convective one occurs near the critical Rayleigh number $Ra_0 \sim 1707.76$. To validate our results, we compute the Nusselt number Nu as a function of the Rayleigh number Ra and we compare the results with the benchmark solutions of Shan, and Clever and Busse. The percentual error in both cases is less than 4%.

For $Ra > Ra_0$ and $Re > 0$ not too large, we have Rayleigh-Bénard convection together with Poiseuille flow, known as Rayleigh-Bénard-Poiseuille flow. In section 4.4, we study this flow and find that for a fixed value of Ra , the Nusselt number Nu is a decreasing function of the Reynolds number Re and there is a transition from RBP flow to Poiseuille flow when $Nu = 1$. Thus, for fixed Re , we find a critical Rayleigh number Ra_c where the flow is RBP when $Ra > Ra_c$ and Poiseuille flow when $Ra < Ra_c$. The main object of this chapter is to extend the study of the transition curve in the $Ra_c - Re$ plane for larger values of Ra and Re . We study Nu as a function of Ra and show that Nu grows as a power law for large values of Ra close to those we found for Rayleigh-Bénard convection. In the last part of this chapter, we present our conclusions.

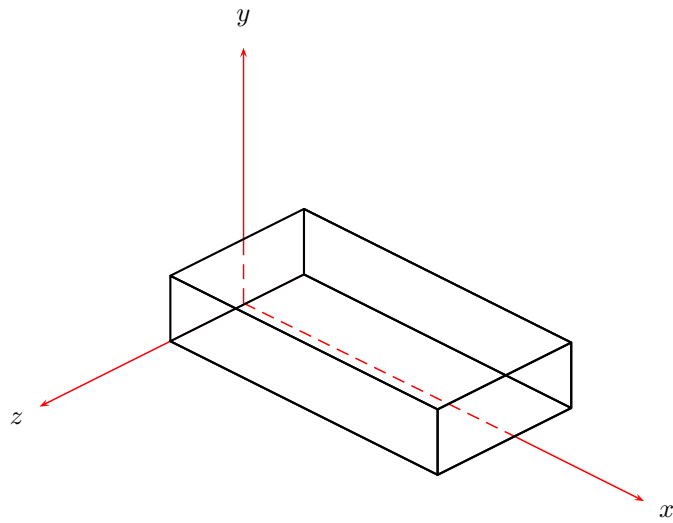


Figure 4.1: Schematic representation of a three dimensional cavity with length L_x , height L_y and width L_z .

4.2 Poiseuille flow

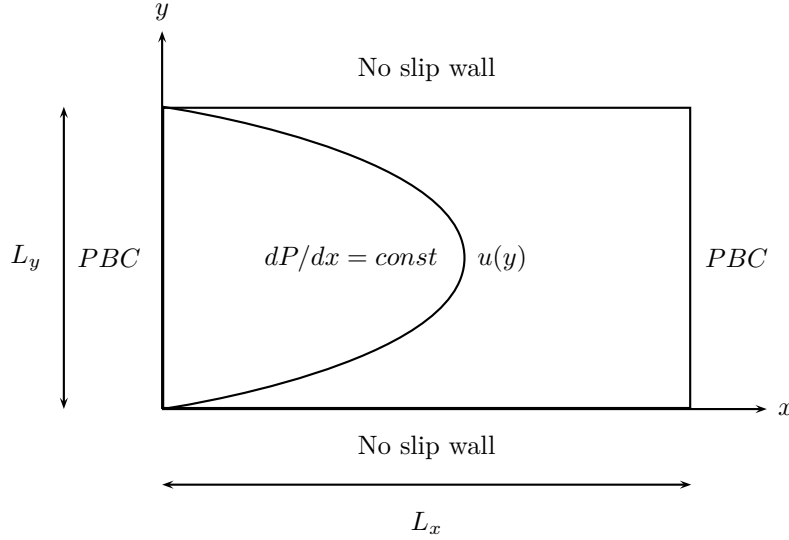


Figure 4.2: Schematic representation of the two dimensional steady state Poiseuille flow with no-slip boundary conditions in the horizontal walls with length L_x and periodic boundary conditions (PBC's) in the vertical walls with height L_y .

In this section, we study the time dependent and steady state plane Poiseuille flow for different Reynolds numbers with the lattice Boltzmann equation method. In order to evaluate the accuracy of our numerical results, we compare them with the analytical solutions in steady and non-steady states.

The flow of a viscous fluid contained in a pipe of constant cross section is referred to as Poiseuille flow [34]. It was experimentally studied by Jean Léonard Marie Poiseuille in 1838 and Gotthilf Heinrich Ludwig Hagen in 1839 [35]. In a two dimensional incompressible plane, Poiseuille flow is a unidirectional flow between two infinite parallel plates, separated by a distance L_y , as shown in figure 4.2. The flow is moving due to a constant pressure gradient in the horizontal direction $dP/dx = 0$. The no-slip boundary conditions are considered, in which the vertical and horizontal components of fluid velocity are equal to those of the bottom and top walls. Since the horizontal walls are at rest, then $\mathbf{u} = 0$.

The momentum conservation equation in the x direction is

$$\frac{\partial u'}{\partial t'} = -\frac{1}{\rho} \frac{dP'}{dx'} + \nu \frac{\partial^2 u'}{\partial y'^2}, \quad (4.1)$$

with u' the horizontal component of the velocity, t' time, y' vertical position, ν the kinematic viscosity, ρ the fluid density, and $-\hat{P}' = -dP'/dx'$ the pressure gradient, in which the negative sign shows that the pressure decreases in the flow direction. Note that the superindex $'$ is used to denote the dimensional parameters.

The initial condition and the no-slip boundary conditions are

$$u(x, y, 0) = 0, \quad 0 \leq x \leq L_x, \quad 0 \leq y \leq L_y. \quad (4.2)$$

$$u(x, 0, t) = 0, \quad u(x, L_y, t) = 0. \quad (4.3)$$

In a steady state the term in the left hand side of equation (4.1) is zero, hence

$$\nu \frac{\partial^2 u'}{\partial y'^2} = \frac{\hat{P}'}{\rho}. \quad (4.4)$$

This equation states that there is a balance between the pressure gradient in the fluid and the viscous shear stress. The general solution for the above equation is

$$u(y)' = \frac{\hat{P}'}{\nu\rho} (y'^2 + ay' + b), \quad (4.5)$$

where a and b are constants that are found from the no-slip boundary conditions on the top and bottom walls. Then,

$$u'^{(s)} = \frac{\hat{P}'}{2\nu\rho} y' (L_y - y'). \quad (4.6)$$

The velocity in the center of the cavity u'_0 is

$$u'_0 = \frac{L_y^2 \hat{P}'}{8\nu\rho}. \quad (4.7)$$

The time dependent solution of equation (4.1) using Fourier series is given by

$$u'(y', t') = u'^{(s)} + \sum_{n=1}^{\infty} C'_n \sin\left(\frac{n\pi y'}{L_y}\right) \exp\left(\frac{-\nu n^2 \pi^2 t'}{L_y^2}\right), \quad (4.8)$$

with

$$C'_n = -\frac{2}{L_y} \int_0^{L_y} u^{(s)'} \sin \frac{n\pi y'}{L_y} dy = \frac{2P'\hat{L}_y^2}{\nu(n\pi)^3} (\cos n\pi - 1). \quad (4.9)$$

The non-dimensional quantities are

$$y = \frac{y'}{L_y}, \quad t = \frac{\nu t'}{L_y^2}, \quad u = \frac{L_y u'}{\nu}, \quad (4.10)$$

where L_y is the characteristic length and L_y^2/ν is the characteristic time. The non-dimensional parameter that measures the ratio of inertial forces to viscous forces is the Reynolds number, given by

$$Re = \frac{u'_0 L_y}{\nu} = u_0, \quad (4.11)$$

with u'_0 the horizontal velocity in the center of the cavity in a steady state given by equation (4.7). Then, substituting u'_0 into the above equation, we obtain

$$Re = \frac{L_y^3 \hat{P}}{8\nu^2 \rho}. \quad (4.12)$$

From this equation, we solve for the pressure gradient \hat{P} and we substitute this term into equation (2.71) to simulate Poiseuille flow.

The dimensionless form of equations (4.6), (4.8) and (4.9) are

$$u^{(s)}(y) = 4Re(1 - y)y, \quad (4.13)$$

$$u(y, t) = u^{(s)}(y) + \sum_{n=1}^{\infty} C_n \sin(n\pi y) \exp(-n^2 \pi^2 t), \quad (4.14)$$

$$C_n = \frac{2\hat{P}}{\nu^2} \left(\frac{L_y}{n\pi} \right)^3 (\cos n\pi - 1). \quad (4.15)$$

In the LBEM, we simulate the no-slip boundary condition with the halfway bounce back boundary condition (HBB), in which the particle distribution functions f_k that hit a wall are reflected in the opposite direction, considering that the wall is placed in the middle of two lattice nodes [36, 37, 38]. The vertical walls have periodic boundary conditions, PBC, where the outgoing particle distribution functions f_k enter on the

opposite wall. This boundary condition simulates a system periodically infinite in the horizontal direction.

In figure 4.3(a), we show the normalized velocity profile u/Re as a function of the height y for $Re = 1,000$ at $x = 1/2$ and different times t together with the solution of equation (4.14), continuous colored curves. For larger times t , the series expansion in equation (4.14) is zero and the velocity profile reaches the steady state given by equation (4.13). The maximum velocity $u(y) = Re$ at $y = L_y/2$.

In figure 4.3(b), we show the normalized velocity profile u/Re at $x = 1/2, y = 1/2$ as a function of time t for four values of Re together with equation (4.14), continuous curve in black. We show that our results are in good agreement with the solution of equation (4.14).

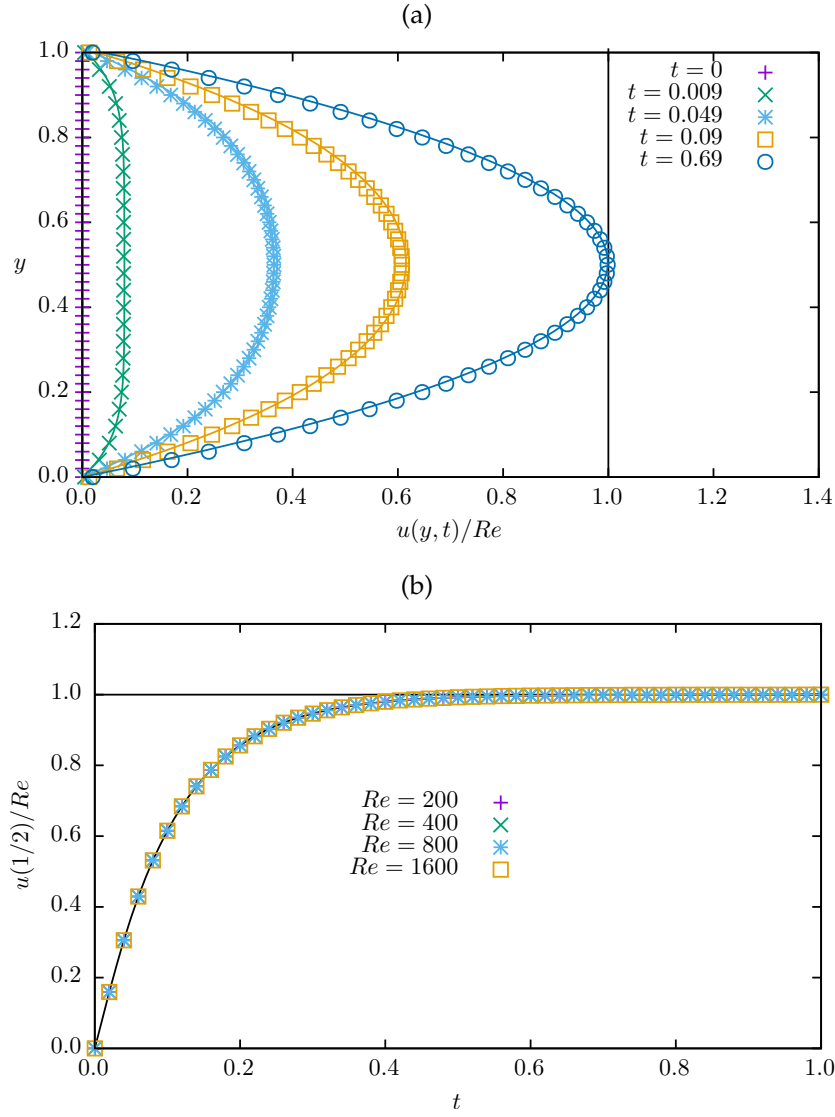


Figure 4.3: (a) For $Re = 1,000$, the normalized velocity profiles u/Re as a function of the height y at $x = 1/2$ and several times t together with the solution of equation (4.14), continuous colored curves. The average percentual error of the solutions in steady states is 3.8%. (b) The normalized velocity profile u/Re at $x = 1/2, y = 1/2$ as a function of time t for different Reynolds numbers Re together with the graph of equation (4.14), continuous curve in black. In the numerical solutions, $n = 200, \tau = 0.6, \rho = 1$, the number of mesh sites in L_y is $N_y = 101$.

4.3 Rayleigh-Bénard convection

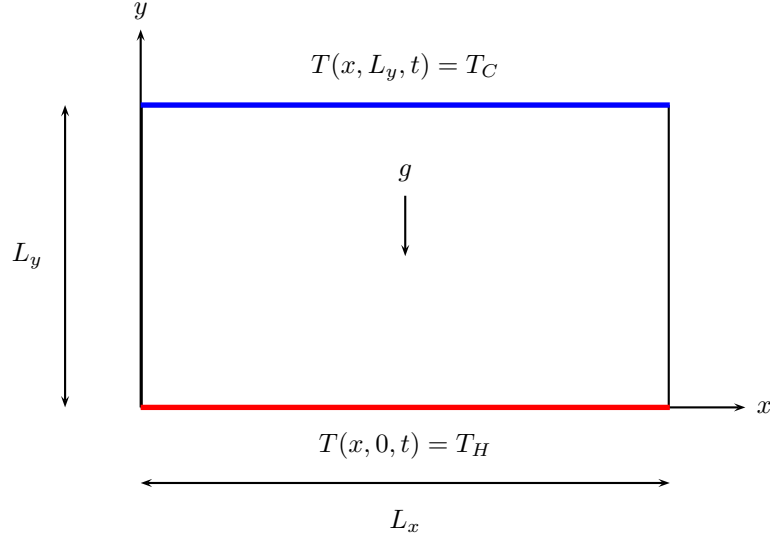


Figure 4.4: Schematic representation of the Rayleigh-Bénard convection. The cavity has length L_x and height L_y with $L_x = L_y/2$. The acceleration due to gravity g points vertically downwards. The bottom and top walls are at constant temperatures T_H and T_C , respectively, with $T_H > T_C$.

In this section, we study the Rayleigh-Bénard convection with the lattice Boltzmann equation method with two distribution functions, one for the particles and the other one for the temperature. This problem consists of a fluid that is confined between two plates that are thermally conducting. The bottom and top plates are at constant temperatures T_H and T_C , respectively, with $T_H > T_C$. The cavity has a length L_x and a height L_y as is shown in figure 4.4. As the temperature difference between the two plates is raised, the system reaches the convective state at the critical Rayleigh number Ra_0 and regular patterns are formed, known as Bénard cells. At $Ra < Ra_0$, the system remains in the conductive state.

The Rayleigh-Bénard convection studies are carried out in the framework of the Boussinesq approximation, in which is considered that all the properties of the fluid are constant except in the buoyancy term, where the density of the fluid is assumed to be a linear function of the

temperature

$$\rho = \rho_0(1 - \beta(T - T_0)), \quad (4.16)$$

where ρ_0 is the average fluid density, T_0 is a reference temperature and β the coefficient of the thermal expansion. Then, the gravity is written as

$$\mathbf{G} = \rho_0 \mathbf{g} - \rho \mathbf{g} \beta (T - T_0), \quad (4.17)$$

where \mathbf{g} is the acceleration due to gravity. Note that the first term of the right hand side of the above equation is absorbed into the pressure term. Hence, the Boussinesq equations are

$$\nabla \cdot \mathbf{u}' = 0 \quad (4.18a)$$

$$\frac{\partial \mathbf{u}'}{\partial t'} + \mathbf{u}' \cdot \nabla \mathbf{u}' = -\frac{\nabla P'}{\rho} + \nu \nabla^2 \mathbf{u}' - \mathbf{g} \beta (T' - T_0) \quad (4.18b)$$

$$\frac{\partial T'}{\partial t'} + \nabla \cdot (\mathbf{u}' T') = \alpha \nabla^2 T'. \quad (4.18c)$$

with α the thermal diffusivity and ν the kinematic viscosity.

In what follows, we denote the dimensional parameters of the problem with the superindex $'$. The dimensionless parameters that describe the problem are

$$\mathbf{r} = \frac{\mathbf{r}'}{L_y}, \quad t = \frac{\alpha}{L_y^2} t', \quad \mathbf{u} = \mathbf{u}' \frac{L_y}{\alpha}, \quad T = \frac{T' - T_0}{\Delta T'}, \quad (4.19)$$

with L_y the characteristic length, L_y^2/α the characteristic time and $\Delta T' = T'_H - T_0$ the characteristic temperature with $T_0 = T'_C$ the reference temperature. The Prandtl number and the Rayleigh numbers are

$$Pr = \frac{\nu}{\alpha}, \quad Ra = \frac{g \beta \Delta T L_y^3}{\nu \alpha}. \quad (4.20)$$

In the numerical simulations, the horizontal walls have isothermal, no-slip boundary conditions. We simulate this conditions with the halfway bounce back boundary condition, HBB, where the particle f_k and temperature T_k distribution functions that hit the wall are reflected in the opposite direction [36, 37, 38]. The vertical walls have periodic boundary conditions. At $t = 0$, the flow is at the lower temperature T_C .

To validate the numerical simulations we follow the work of Shan [1]. We study the maximum vertical velocity v_{max} to find the transition from a conductive state to a convective one at $Ra_0 \sim 1,707.76$, the theoretical value predicted by linear stability theory [39, 40].

In figure 4.5(a), we show the maximum vertical velocity v_{max} as a function of time t for four values of Ra . We find that the maximum vertical velocity grows as $v_{max} \propto A \exp(\gamma t)$, with γ the growth rate. The fits are shown as colored curves. From the previous figure, we study the growth rate of the maximum vertical velocity γ as a function of Ra for three values of the relaxation time τ , as we show in figure 4.5(b). The data is fit by $\gamma = aRa + b$, by the colored straight lines. The intersection of each line with the x axis gives us the value of Ra in which the transition occurs. We find that for $\tau = 0.6$, the Rayleigh number $Ra = 1,707.75$, dashed lines in black, agrees well, within a 0.0005%, with the theoretical value Ra_0 . This value of τ is used in all the numerical simulations that follow.

In figure 4.6, we show the temperature field and the isotherms in steady states for three values of Ra . The plumes are symmetric with respect to the vertical axis y .

The Nusselt number Nu measures the ratio of the convective heat transfer to the conductive heat transfer. When the temperature gradient is in the vertical direction, the Nusselt number [6] is

$$Nu = -\frac{L_y}{\Delta T' L_x} \int_0^{L_x} \frac{\partial T'(x', L_y)}{\partial y'} dx'. \quad (4.21)$$

Another equivalent definition of the Nusselt number [2] is

$$Nu = 1 + \frac{\langle v' T' \rangle}{\alpha \Delta T' / L_y}, \quad (4.22)$$

where v' is the vertical component of the velocity and $\langle \rangle$ is the average over the height of the cavity. For conductive heat transfer, $Nu = 1$. When heat is transferred by convection, $Nu > 1$. We measure the Nusselt number Nu given by equation (4.22) in a steady state as a function of the Rayleigh number Ra . Our results compare well with those of Clever and Busse [2], and Shan [1] for large Rayleigh numbers Ra , as we show in figure 4.7.

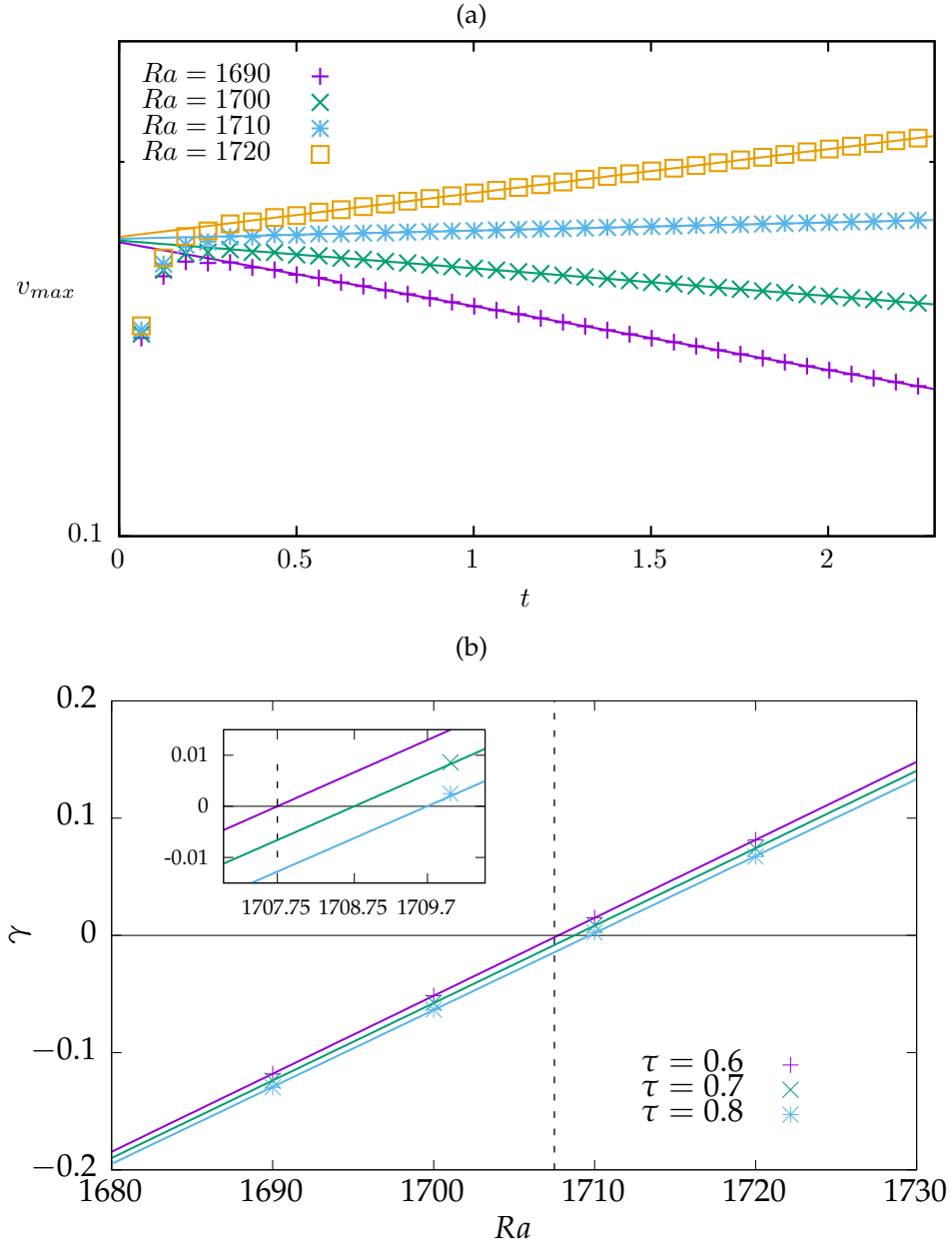


Figure 4.5: (a) The maximum vertical velocity v_{max} as a function of time t for different Rayleigh numbers Ra . The colored continuous curves are the fit of $v_{max} = A \exp(\gamma t)$. (b) The growth rate of the maximum vertical velocity γ as a function of the Rayleigh number Ra for different relaxation times τ . For $\tau = 0.6$, the Rayleigh number $Ra = 1,707.75$, is shown as the vertical dotted line. In the numerical simulations $\rho = 1$, $\tau = 0.6$, $Pr = 0.71$ and the number of mesh sites in L_x, L_y is $N_x = 201, N_y = 101$.

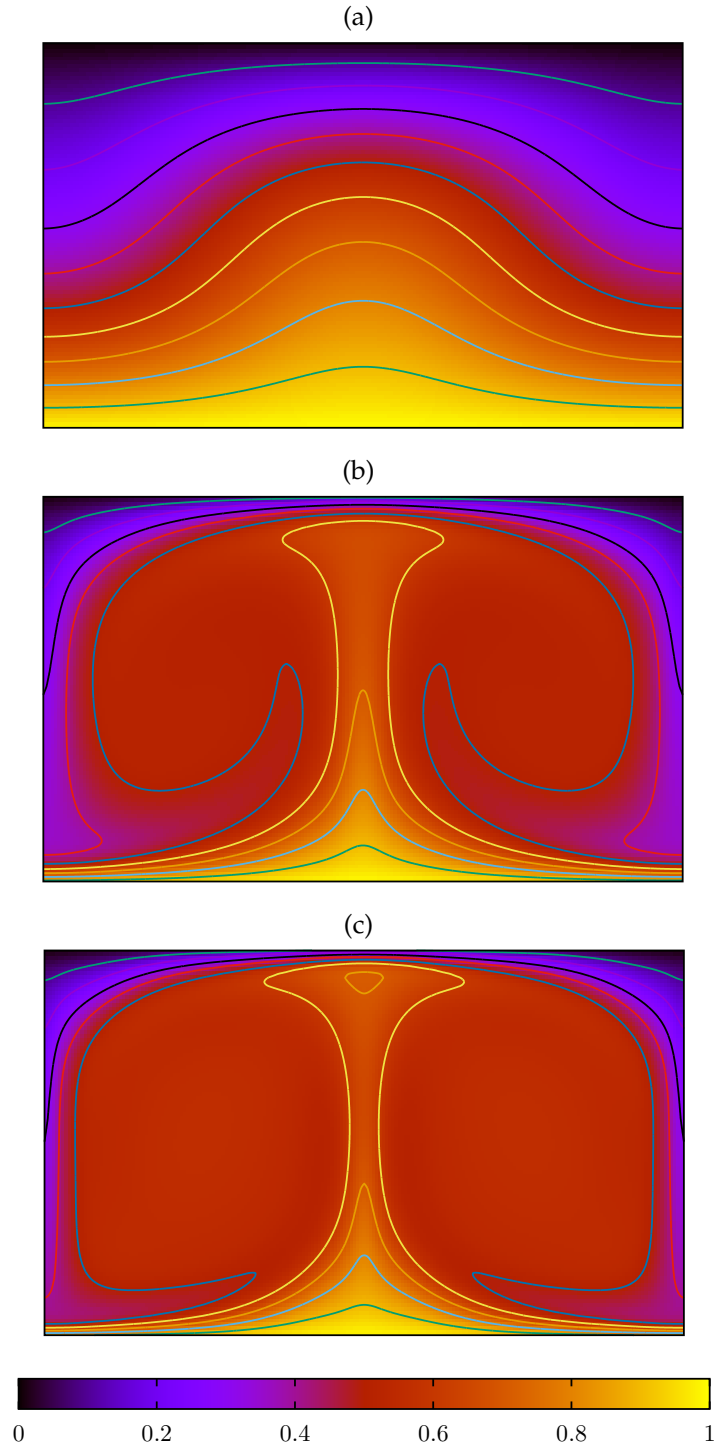


Figure 4.6: The temperature field and the isotherms in steady states for three values of Ra . (a) $Ra = 2 \times 10^3$, (b) $Ra = 2 \times 10^5$ and (c) $Ra = 1 \times 10^6$. There are 10 isotherms between $0 \leq T \leq 1$.

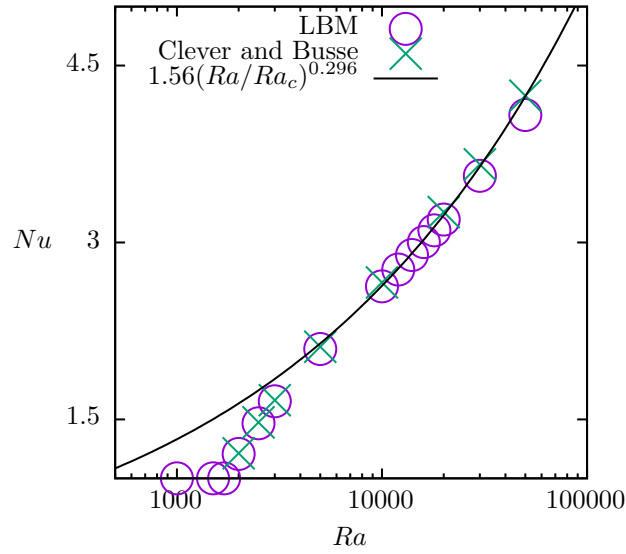


Figure 4.7: The steady state Nusselt number Nu as a function of the Rayleigh number Ra . The Nusselt number grows as $Nu = aRa^b$ with $a = 0.198$ and $b = 0.28$. The LBEM simulations, open circles in magenta, agree with the results of Shan for large Ra , black curve [1], and those of Clever and Busse, green crosses [2]. In both cases, the percentual error is less than 4% for $5,000 \leq Ra \leq 50,000$.

4.4 Rayleigh-Bénard-Poiseuille flow

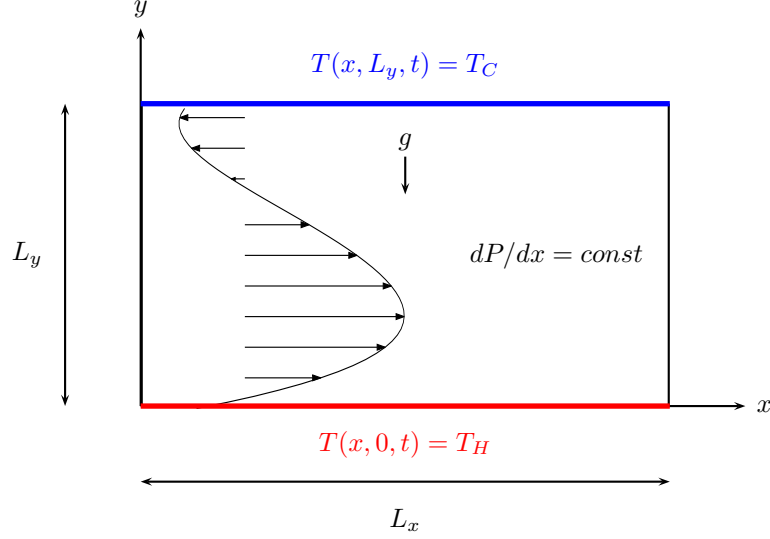


Figure 4.8: Schematic representation of the Rayleigh-Bénard-Poiseuille (RBP) flow. The cavity has a length L_x and a height L_y with $L_y = L_x/2$. The fluid is driven by a pressure difference in the x direction and a temperature difference in the y direction. The bottom temperature T_H and the top temperature T_C with $T_H > T_C$. The acceleration due to gravity g points vertically downwards.

In this section, we study the Rayleigh-Bénard-Poiseuille flow (RBP), which is a combination of Rayleigh-Bénard convection and Poiseuille flow presented in the previous sections. There is a pressure difference in the horizontal direction, characterized by the Reynolds number Re and a temperature difference in the vertical direction, characterized by the Rayleigh number Ra . For a fixed value of Re , $Re > 0$, and $Ra < Ra_0$, we find a Poiseuille flow and as Ra grows, we find a transition at a critical value of the Rayleigh number Ra_c where the flow is the RBP. In what follows, we study this transition for a wide range of Reynolds Re and Rayleigh Ra numbers.

We consider two infinite parallel plates separated by a distance L_y . The bottom and top plates are maintained at constant temperatures T_H and T_C , respectively, with $T_H > T_C$. A constant pressure gradient $\partial P/\partial x = 0$ is

imposed in the horizontal direction. In figure 4.8, we show the schematic representation of RBP flow. The bottom and top walls have no-slip boundary conditions. With the Boussinesq approximation, the governing equations are

$$\nabla \cdot \mathbf{u}' = 0 \quad (4.23a)$$

$$\frac{\partial \mathbf{u}'}{\partial t'} + \mathbf{u}' \cdot \nabla \mathbf{u}' = -\frac{\nabla P'}{\rho} + \nu \nabla^2 \mathbf{u}' - \mathbf{g}\beta(T' - T_0) \quad (4.23b)$$

$$\frac{\partial T'}{\partial t'} + \nabla \cdot (\mathbf{u}' T') = \alpha \nabla^2 T'. \quad (4.23c)$$

with α the thermal diffusivity and ν the kinematic viscosity. The dimensionless parameters are

$$t = \frac{t' \nu}{L_y^2}, \quad \mathbf{u} = \mathbf{u}' \frac{L_y}{\nu}, \quad T = \frac{T' - T'_C}{T'_H - T'_C}, \quad (4.24)$$

where L_y is the characteristic distance, L_y^2/ν the characteristic time and $T'_H - T'_C$ the characteristic temperature. Note that the dimensional parameters of the problem are denoted with the superindex $'$.

We perform the numerical simulations of the bidimensional RBP flow with the LBEM. The no-slip boundary conditions are simulated with the halfway bounce back boundary conditions that we have described in previous sections. The vertical walls have periodic boundary conditions. The aspect ratio of the cavity is $r = L_y/L_x = 1/2$. The pressure gradient is constant along the cavity. At $t = 0$, the temperature in the fluid is T_C .

For $Ra = 10,000$ and $Re = 40$, a mesh refinement was performed. The number of mesh sites of the computational domain in L_x, L_y is N_x, N_y . We measure the Nusselt number Nu given by equation (4.22) in a steady state and we calculate the percentual error e given by equation (4.25) for different values of the number of mesh sites, taking as a reference the value of Nu of the finer mesh. The results are shown in table 4.1. We show that Nu tends toward a well defined value as the number of mesh sites of the computational domain increases. For $N_x = 201, N_y = 101$, we find that the percentual error is less than 0.4. This value of N_y is used in all the numerical simulations that follow, except where noted.

$$e = \frac{Nu(N_{y_{max}}) - Nu(N_y)}{Nu(N_{y_{max}})} \times 100. \quad (4.25)$$

Table 4.1: The Nusselt number Nu in a steady state for different values of the number of mesh sites N_x, N_y together with the percentual error e for $Ra = 10,000$ and $Re = 40$. In the numerical simulations the parameters are $\rho = 1$, $\tau = 0.6$ and $Pr = 0.71$.

N_y	Nu	e
51	2.477	1.02
76	2.488	0.58
101	2.493	0.37
126	2.497	0.25
151	2.499	0.17
176	2.500	0.11
201	2.501	0.07
226	2.503	0.0

In figure 4.9, we show the horizontal component of the velocity u as a function of the height y together with the steady state solution of Poiseuille flow, continuous curve in black, given by equation (4.13). In figure 4.9(a), we show u as a function of y for Reynolds number $Re = 10$ and three different Rayleigh numbers Ra . For $Ra < Ra_0$, shown as crosses in magenta, the velocity profile is in a steady state and the result compares well, within a 4.8% with the steady state solution of Poiseuille flow. For $Ra \geq Ra_0$, after a time has passed, the velocity profiles are not longer symmetric with respect to the vertical axis y and they yield a quasi steady state for which the velocity profiles fluctuate periodically. This is shown in figure 4.9(b) for $Re = 10$, $Ra = 2,000$ and several times t .

In figure 4.10, we show the velocity fields in periodic steady states in the first column, together with the vertical component of the velocity v as a function of the horizontal component u in the second column, at $x = 1/2$ and $y = 1/2, 1/4, 3/4$ for $Ra = 20,000$ and four values of Re . In figure 4.11, we show the corresponding temperature fields and the isotherms of the previous figure. In figures 4.10(b), (d), (f) and (h), the trajectories in the $u - v$ space are closed and there is a symmetry between them at $y = 1/4$ and $y = 3/4$. In figure 4.12, we show the vertical velocity component v as a function of the horizontal component u at the center of the cavity in a

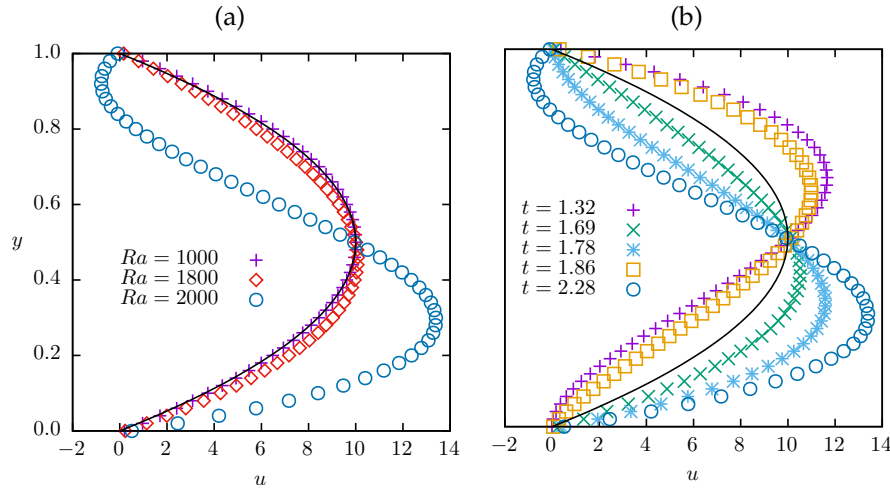


Figure 4.9: The horizontal component of the velocity u as a function of the height y together with the steady state solution of Poiseuille flow, shown as the continuous curve in black, given by equation (4.13). (a) The horizontal velocity u as a function of y in a periodic steady state for Reynolds number $Re = 10$ and different Rayleigh numbers Ra . (b) The horizontal velocity u as a function of y for $Ra = 2,000$, $Re = 10$ and different times t . In terms of dimensional variables, the parameters are $N_x = 201$, $N_y = 101$, $\rho = 1$, $\tau = 0.6$, $Pr = 0.71$, $\beta = 0.1$ and $g = 0.001$. We keep these values for most of the numerical simulations, except where noted.

periodic steady state for the same Rayleigh number of the previous figure and several values of Re . The period of oscillation in the x direction is twice that of the one in the y direction at $y = 1/2$, $v \rightarrow 0$ and $u \rightarrow Re$. In figures 4.10(a), (c), (e) and (g), we show that for small Re , the presence of Poiseuille flow breaks the symmetry of the convective rolls, as a consequence they shift downstream to the right. For larger Re , the Poiseuille flow stabilizes the conductive state.

In figure 4.13, we show the power spectra P of u and v as functions of the frequency f in the center of the cavity in a periodic steady state for $Ra = 20,000$ and $Re = 50$. In figure 4.14, we show the fundamental frequencies of u , f_u , in (a) and v , f_v in (b) as functions of Re for different values of Ra . The data grows linearly with Re ,

$$f = mRe, \quad (4.26)$$

and $f_u = 2f_v$. In figure 4.15, we show that m as a function of Ra decreases as Ra grows.

To find the transition between RBP flow to Poiseuille flow for a fixed value of Ra as Re changes, we evaluate the Nusselt number Nu knowing that $Nu > 1$ in a RBP flow and $Nu = 1$ in a Poiseuille flow.

In figure 4.16, we show Nu in a steady state as a function of Re for four values of Ra . Then for each value of Ra , we can find Re_c as mentioned above. Another equivalent way is to fix Re and change Ra starting with a small value for which $Nu = 1$ and finding Ra_c as the value where RBP flow passes to a Poiseuille flow.

In figure 4.17, we show the critical Rayleigh number Ra_c as a function of the Reynolds number Re for different values of the number of mesh sites in L_x , L_y . To the left and above of this curve, the flow is RBP and to the right and below, the flow is Poiseuille. The data is fitted for $Re \leq 50$, $Ra_c = aRe^2 + bRe + c$ with $c \approx 1,708$, shown by the dotted curves in black and for $Re \geq 50$, $Ra_c = a_1Re^2 + b_1Re + c_1$, shown by the continuous curves in black.

Finally, we show the Nusselt number Nu as a function of the Rayleigh number Ra for fixed values of the Reynolds number Re in figure 4.18. Our results show that for large values of Ra , $Nu = aRa^b$ where a and b are two constants. For $Re = 0$, the results are in good agreement with those of Shan [1], and Clever and Busse [2] presented in section 4.3.

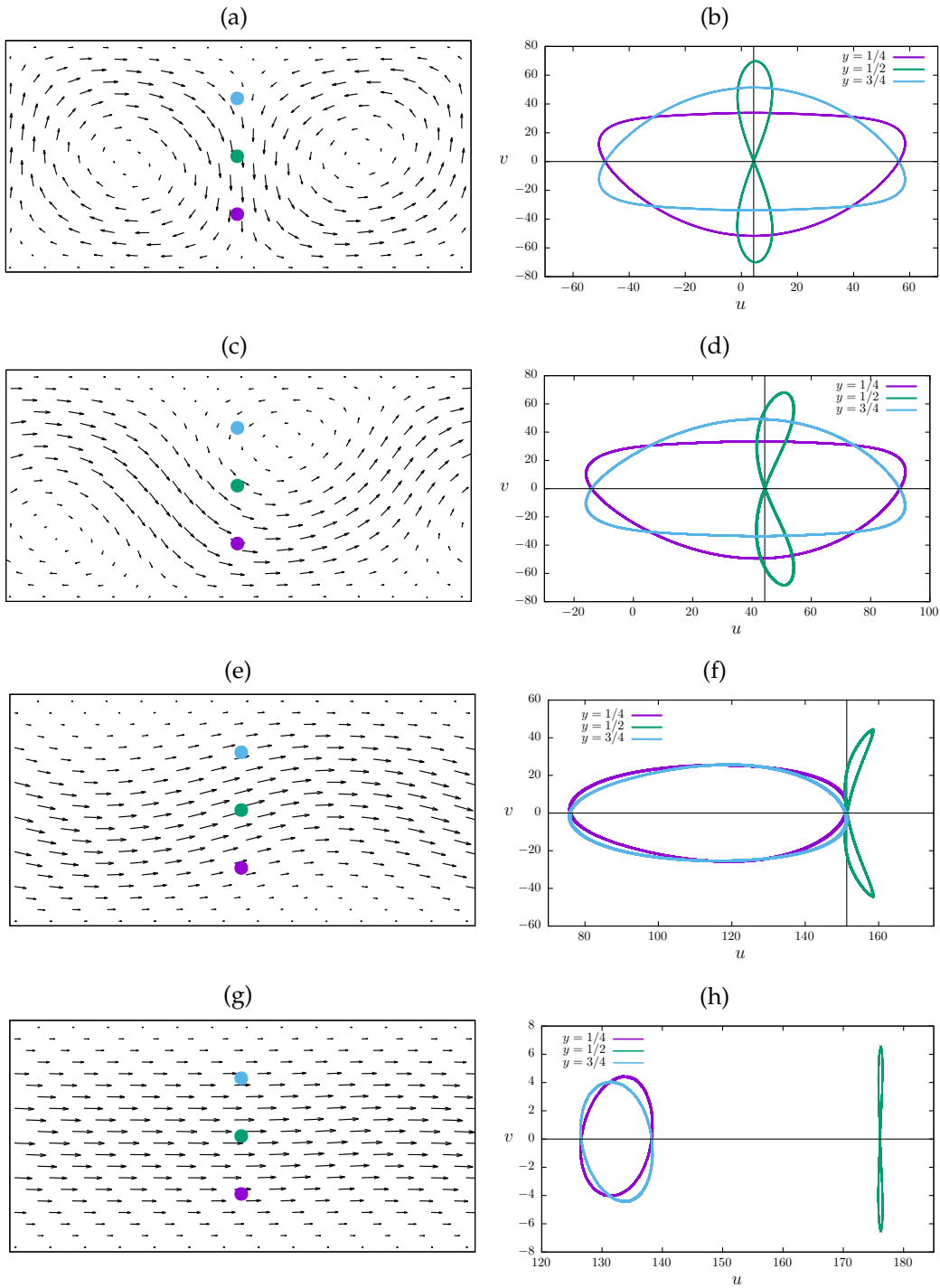


Figure 4.10: The velocity fields in periodic steady states in the first column together with the vertical velocity v as a function of the horizontal velocity u in the second column, at $x = 1/2$ and different heights of the cavity y , for Rayleigh number $Ra = 20,000$. (a) and (b) $Re = 5$, (c) and (d) $Re = 50$, (e) and (f) $Re = 150$, and (g) and (h) $Re = 175$.

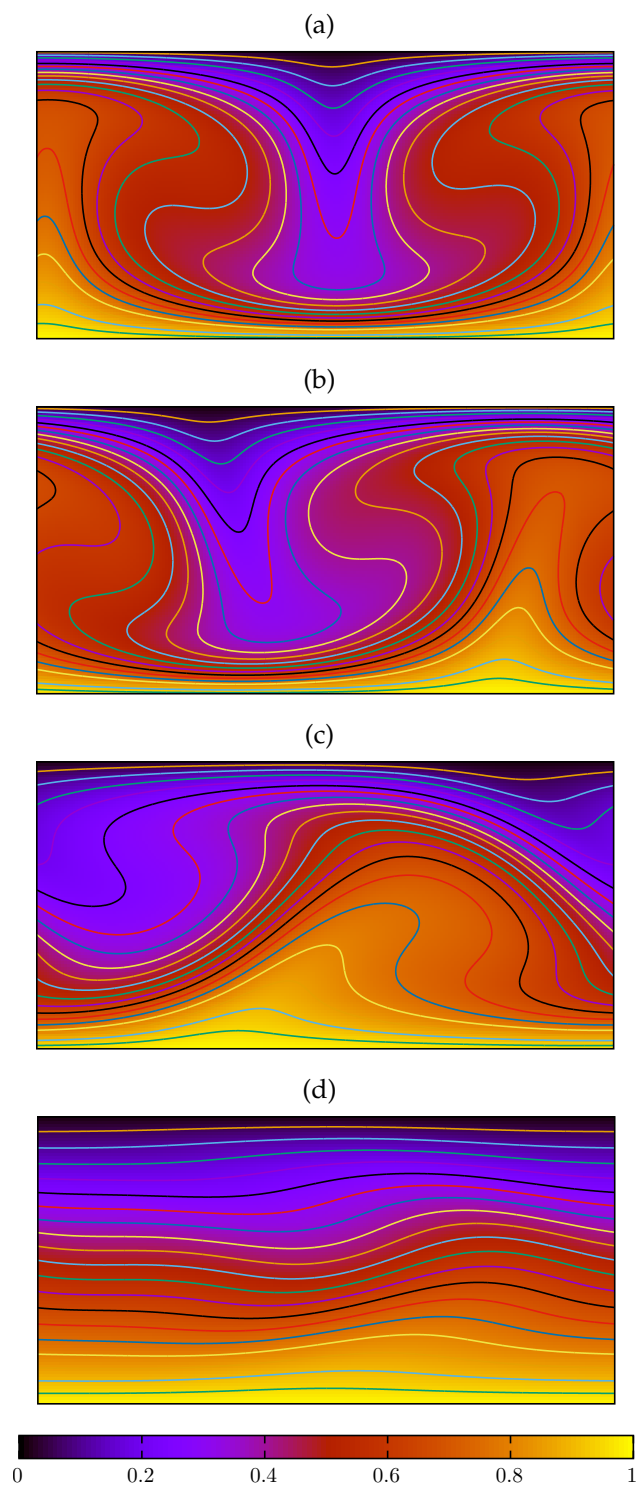


Figure 4.11: The temperature field and the isotherms in periodic steady states for $Ra = 20,000$ and the same values of Re of the previous figure. There are 20 isotherms between $0 \leq T \leq 1$.

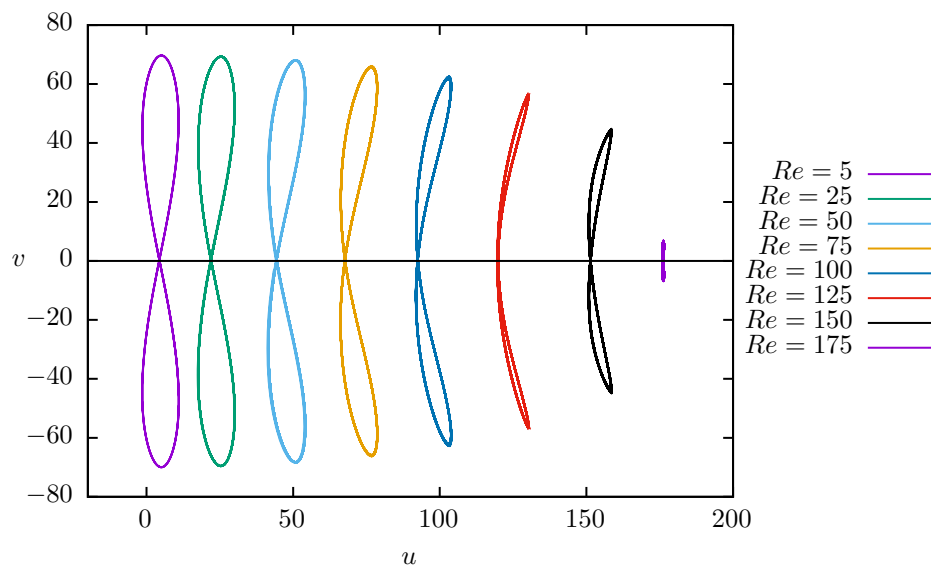


Figure 4.12: The vertical velocity v as a function of the horizontal velocity u at $x = 1/2, y = 1/2$ and $Ra = 20,000$, after a time transient for different values of the Reynolds number Re .

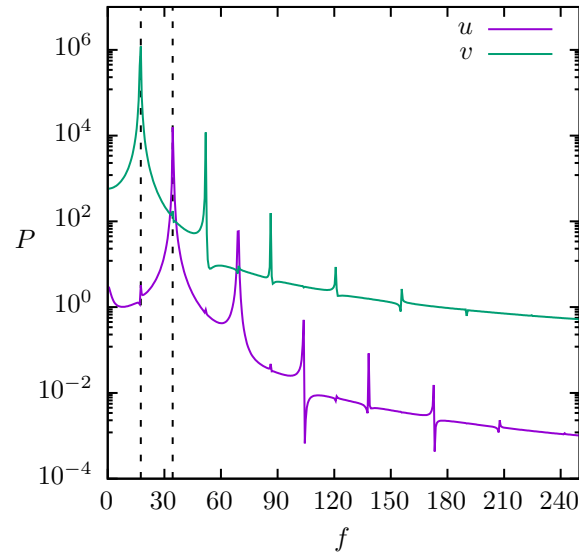


Figure 4.13: The Power spectra P as a function of the frequency f for $Ra = 20,000$ and $Re = 50$. The horizontal velocity component u , continuous line in magenta together with the vertical velocity component v , continuous line in green. The fundamental frequencies for u and v are $f_u = 34.42$, shown as the vertical dashed line on the right and $f_v = 17.48$, shown as the vertical dashed line on the left.

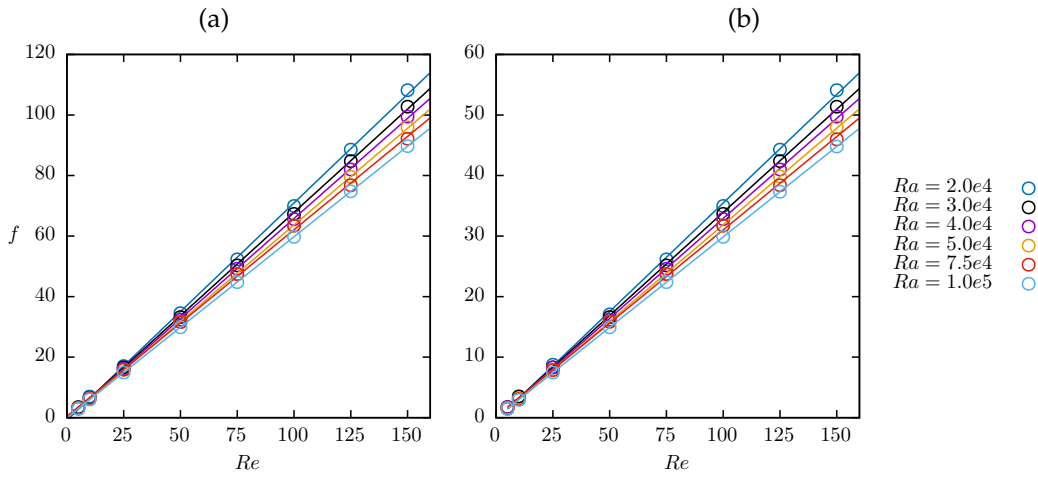


Figure 4.14: The fundamental frequency f of the velocity components u and v as a function of the Reynolds number Re for six values of the Rayleigh numbers Ra at $x = 1/2, y = 1/2$. (a) f as a function of Re of the horizontal velocity component u . (b) f as a function of Re for the vertical component v . The fundamental frequency f is fit by $f = mRe$ with $f_u = 2f_v$.

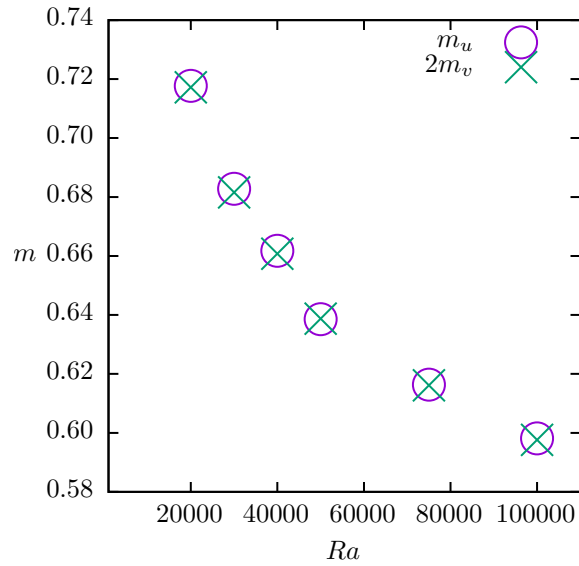


Figure 4.15: The slope of equation (4.26) of the horizontal component of the velocity m_u together with the slope of equation (4.26) of the vertical component m_v as a function of the Rayleigh number Ra .

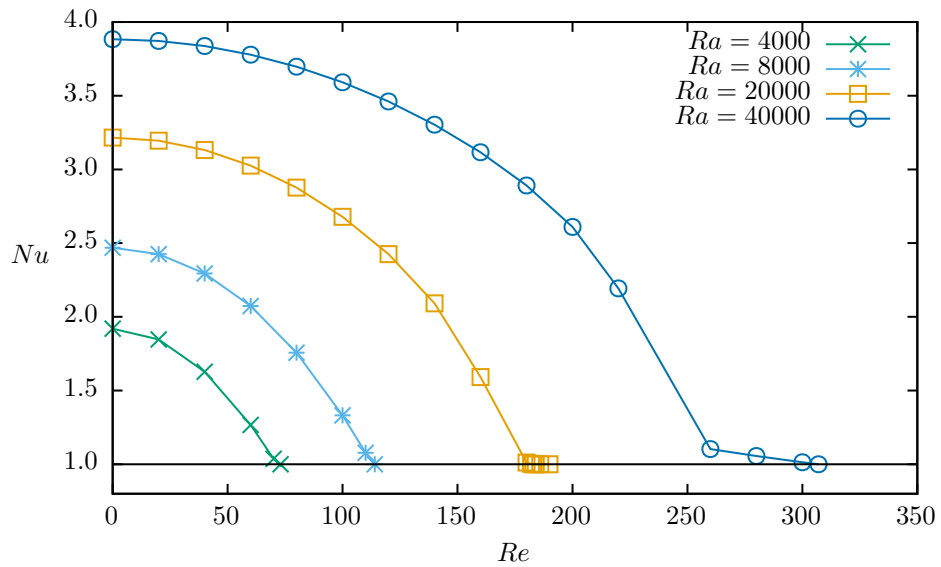


Figure 4.16: The Nusselt number Nu , calculated with equation (4.22), in a steady state as a function of the Reynolds number Re for five values of Rayleigh number Ra .

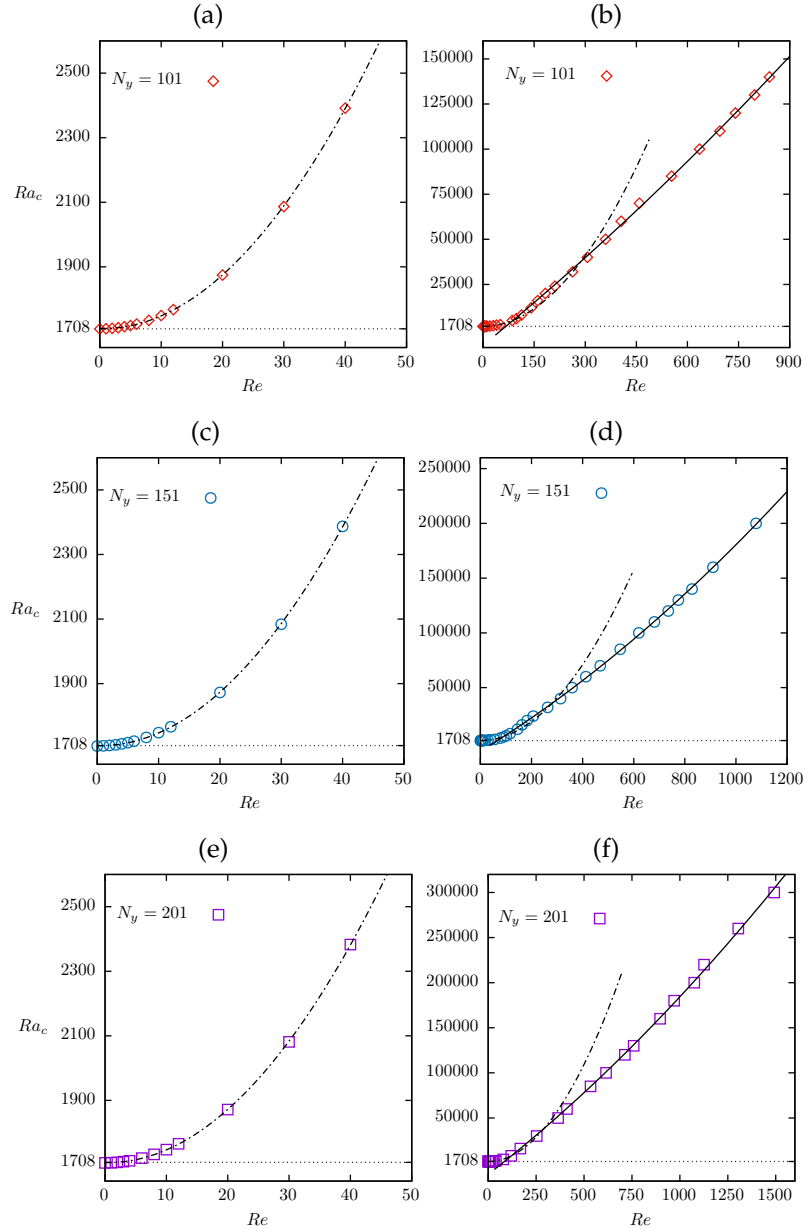


Figure 4.17: The critical Rayleigh number Ra_c as a function of the Reynolds number Re for different mesh sizes. For $Re \leq 50$ the data grows as $Ra_c = aRe^2 + bRe + c$ with $c \approx 1,708$, shown as the dotted curves in black. For $Re \geq 50$ the data grows as $Ra_c = a_1Re^2 + b_1Re + c_1$, shown as the continuous curves in black. (a) For $N_y = 101$ and $Re \leq 50$, $a = 0.43$, $b = -0.43$ and $c = 1708.86$. (b) For $Re \geq 50$, $a_1 = 0.02$, $b_1 = 153.73$ and $c_1 = -8735.6$. (c) For $N_y = 151$ and $Re \leq 50$, $a = 0.43$, $b = -0.41$ and $c = 1,707.85$. (d) For $Re \geq 50$, $a_1 = 0.04$, $b_1 = 143.3$ and $c_1 = -8,056.9$. (e) For $N_y = 201$ and $Re \leq 50$, $a = 0.43$, $b = -0.4$ and $c = 1,707.42$. (f) For $Re \geq 50$, $a_1 = 0.03$, $b_1 = 165.1$ and $c_1 = -12,481.1$.

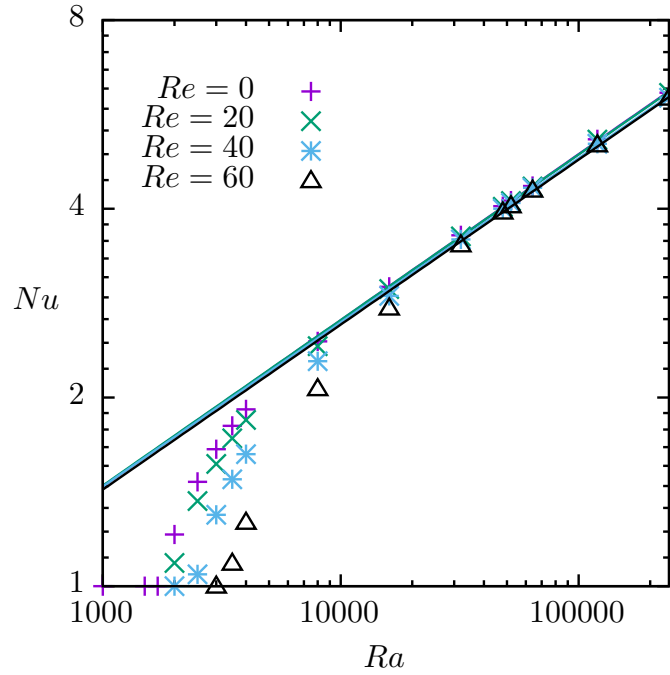


Figure 4.18: The Nusselt number Nu as a function of the Rayleigh number Ra for four values of the Reynolds number Re . For large values of Ra , Nu grows as $Nu = aRa^b$. For $Re = 0$ with $a = 0.231$ and $b = 0.264$, for $Re = 20$ with $a = 0.233$ and $b = 0.264$, for $Re = 40$ with $a = 0.236$ and $b = 0.261$, and for $Re = 60$ with $a = 0.231$ and $b = 0.263$.

4.5 Conclusions

In this chapter we studied the Poiseuille, Rayleigh-Bénard and Rayleigh-Bénard-Poiseuille (RBP) flows with the LBEM in the $D2Q9$ model. The numerical results of Poiseuille flow were in good agreement with the analytic solution in steady and non-steady states. The average percentual error for the solution in a steady state was 3.8%.

The study of Rayleigh-Bénard convection showed that for $\tau = 0.6$, the critical Rayleigh number is close to the critical value Ra_0 predicted by linear stability theory. We found that the Nusselt number grows as $Nu = aRa^b$ with Ra the Rayleigh number in agreement with benchmark results[1, 2] with a percentual error less than 4% for $5,000 \leq Ra \leq 50,000$. These comparison showed that the LBEM is an accurate numerical method to simulate fluid flows with heat transfer.

In section 4.4, we studied the RBP flow. For $Re > 0$ and $Ra > Ra_0$, the Poiseuille flow breaks the symmetry of the convection rolls and they move downstream to the right. In a periodic steady state, the trajectories of the velocity components u and v are closed and there is a symmetry between their trajectories at $L_y = 1/4$ and $L_y = 3/4$ with L_y the height of the cavity. The velocity $\mathbf{v} = (u, v)$ at any point $(x, L_y/2)$ oscillates in time in a way that the frequency of u is twice that of v . The Nusselt number as a function of the Reynolds number showed that for a fixed value of Ra , the transition between the RBP flow and Poiseuille flow is found when Nu reaches the conductive state at $Nu = 1$. We studied the transition curve for different values of the number of mesh sites in L_x, L_y . In the largest mesh size, we went to Rayleigh and Reynolds numbers $Ra \leq 300,000$ and $Re \leq 1,500$, respectively. To go to higher Ra and Re numbers, it is necessary to consider larger domains. We found that the $Ra_c - Re$ plane has two regions, as shown in figure 4.17. In the left top region, we find the RBP flow. In the right bottom region, we find the Poiseuille flow. For $Re \leq 50$, the data grows as $Ra_c \approx aRe^2 + bRe + 1708$. At $Re = 0$, the value of the Rayleigh number is close to $Ra_0 \sim 1707.76$ for all the cavity sizes. For $Re \geq 50$, the data grows as $Ra_c = a_1Re^2 + b_1Re + c_1$, in this equation the quadratic part is small for all the cavity sizes but not small enough to be ignored.

The transition curve can be built from a different approach, for instance by calculating the heat flow through the vertical axis of the cavity, given

by

$$H = \frac{L_x}{\Delta T' L_y} \int_0^{L_y} \frac{\partial T'(L_x/2, y')}{\partial x'} dy'. \quad (4.27)$$

At the value of Re in which the transition from convective to a conductive flow occurs, the heat flow H will be zero. Since the vertical walls have periodic boundary conditions, H can be evaluated on any vertical line inside the cavity.

Chapter 5

Conclusions

In this thesis, we presented the lattice Boltzmann equation method (LBEM) in the $D2Q9$ model to study flows with heat transfer using two coupled distribution functions, one for the particles and one for the temperature.

In chapter 1, we presented the motivation of studying heat conduction in solids and the Rayleigh-Bénard-Poiseuille flow (RBP).

In chapter 2, we presented the Boltzmann's transport equation which describes the irreversible relaxation towards equilibrium in an isolated system. We showed the equilibrium distribution function given by the Maxwell-Boltzmann distribution function and its approximations to low Mach numbers. We presented the BGK approximation for the collision term, in which the collision integral is replaced by a relaxation to the local equilibrium term and we discussed the discretization in time of this approximation. We obtained the hydrodynamic moments of the equilibrium distribution function, we discussed the discretization of the phase space and we obtained the LBEM in the $D2Q9$ model for the velocity and temperature fields. We obtained the Navier-Stokes equations for fluid flow and convection-diffusion equation for heat and mass transfer through the Chapman and Enskog expansion.

In chapter 3, we showed that heat transfer problems in solids can be simulated by the LBEM with the temperature distribution function. We

studied the heat conduction in a two dimensional solid that is heated from below. We calculated the heat flux in the vertical direction as a function of time. We used Fourier's Law to find a relation between the relaxation time for the temperature field and the thermal conductivity. We compared our results with the analytic solution in steady and non-steady states. We presented the heat transfer in a bidimensional block made of two solids, one on the top of the other with different thermal diffusivities. The results were in good agreement with the analytic solution in a steady state.

In chapter 4 section 4.2, we studied the Poiseuille flow. The numerical results were in good agreement with the analytic solution in steady and non-steady states. In section 4.3, we studied the Rayleigh-Bénard convection. We found that for $\tau = 0.6$, the critical Rayleigh number is close to the critical value predicted by linear stability theory. We showed that the Nusselt number grows as $Nu = aRa^b$ with Ra the Rayleigh number in agreement with benchmark results [1, 2].

In section 4.4, we studied the Rayleigh-Bénard-Poiseuille flow. We found that For $Re > 0$ and $Ra > Ra_0$, Poiseuille flow breaks the symmetry of the convection rolls and that they move downstream to the right. In a periodic steady state, the trajectories of the velocity components u and v are closed and there is a symmetry between them at $L_y = 1/4$ and $L_y = 3/4$ with L_y the height of the cavity. The velocity $\mathbf{v} = (u, v)$ at any point $(x, L_y/2)$ oscillates in time in a way that the frequency of u is twice that of v . The Nusselt number as a function of the Reynolds number showed that for a fixed value of Ra , the transition between the RBP flow and Poiseuille flow is found when Nu reaches the conductive state at $Nu = 1$. We studied that Rayleigh number as a function of the Reynolds number for different cavity sizes. In the largest cavity size, we went to Rayleigh and Reynolds numbers $Ra \leq 300,000$ and $Re \leq 1,500$, respectively. We found that to go to higher Ra and Re numbers, it is necessary to consider larger domains. In figure 4.17, we found that the $Ra_c - Re$ plane has two regions. To the left and above, we find the RBP flow and to the right and below, we find the Poiseuille flow. For $Re \leq 50$, the data grows as $Ra_c \approx aRe^2 + bRe + 1708$. At $Re = 0$, the value of the Rayleigh number is close to $Ra_0 \sim 1707.76$ for all the cavity sizes. For $Re \geq 50$, the data grows as $Ra_c = a_1Re^2 + b_1Re + c_1$, in this equation the quadratic part is small for all the mesh sizes but not small enough to be ignored.

The study of the RBP flow could improve the understanding of

different processes related to renewable energies, such as chemical vapor deposition (CVD) reactors to manufacture solar cells and the cooling in electronic components, to name a few.

Bibliography

- [1] Xiaowen Shan. Simulation of Rayleigh-Bénard convection using a lattice Boltzmann method. *Physical review E*, 55(3):2780, 1997.
- [2] RM Clever and FH Busse. Transition to time-dependent convection. *Journal of Fluid Mechanics*, 65(4):625–645, 1974.
- [3] Emeric Grandjean and Peter A Monkewitz. Experimental investigation into localized instabilities of mixed Rayleigh-Bénard-Poiseuille convection. *Journal of fluid mechanics*, 640:401–419, 2009.
- [4] Xavier Nicolas, Abdelkader Mojtabi, and Jean Karl Platten. Two-dimensional numerical analysis of the Poiseuille-Bénard flow in a rectangular channel heated from below. *Physics of Fluids*, 9(2):337–348, 1997.
- [5] G Barrios, R Rechtman, J Rojas, and R Tovar. The lattice Boltzmann equation for natural convection in a two-dimensional cavity with a partially heated wall. *Journal of Fluid Mechanics*, 522:91–100, 2005.
- [6] Annunziata D’Orazio, Massimo Corcione, and Gian Piero Celata. Application to natural convection enclosed flows of a lattice Boltzmann BGK model coupled with a general purpose thermal boundary condition. *International Journal of Thermal Sciences*, 43(6):575–586, 2004.
- [7] Zhaoli Guo, Baochang Shi, and Chuguang Zheng. A coupled lattice BGK model for the Boussinesq equations. *International Journal for Numerical Methods in Fluids*, 39(4):325–342, 2002.

- [8] Xiaoyi He, Shiyi Chen, and Gary D Doolen. A novel thermal model for the lattice Boltzmann method in incompressible limit. *Journal of computational physics*, 146(1):282–300, 1998.
- [9] Takaji Inamuro, Masato Yoshino, Hiroshi Inoue, Riki Mizuno, and Fumimaru Ogino. A lattice Boltzmann method for a binary miscible fluid mixture and its application to a heat-transfer problem. *Journal of Computational Physics*, 179(1):201–215, 2002.
- [10] J Hardy, Yves Pomeau, and O De Pazzis. Time evolution of a two-dimensional model system. i. invariant states and time correlation functions. *Journal of Mathematical Physics*, 14(12):1746–1759, 1973.
- [11] Uriel Frisch, Brosl Hasslacher, and Yves Pomeau. Lattice-gas automata for the Navier-Stokes equation. *Physical Review Letters*, 56(14):1505, 1986.
- [12] Guy R McNamara and Gianluigi Zanetti. Use of the Boltzmann equation to simulate lattice-gas automata. *Physical Review Letters*, 61(20):2332, 1988.
- [13] Prabhu Lal Bhatnagar, Eugene P Gross, and Max Krook. A model for collision processes in gases. i. small amplitude processes in charged and neutral one-component systems. *Physical review*, 94(3):511, 1954.
- [14] Yue-Hong Qian, Dominique d’Humières, and Pierre Lallemand. Lattice BGK models for Navier-Stokes equation. *EPL (Europhysics Letters)*, 17(6):479, 1992.
- [15] Shiyi Chen and Gary D Doolen. Lattice Boltzmann method for fluid flows. *Annual review of fluid mechanics*, 30(1):329–364, 1998.
- [16] MT Ouazzani, Jean-Paul Caltagirone, Gilles Meyer, and Abdelkader Mojtabi. Etude numerique et expérimentale de la convection mixte entre deux plans horizontaux à températures différentes. *International journal of heat and mass transfer*, 32(2):261–269, 1989.
- [17] HW Müller, M Lücke, and M Kamps. Convective patterns in horizontal flow. *EPL (Europhysics Letters)*, 10(5):451, 1989.

- [18] Mori Yasuo and Uchida Yutaka. Forced convective heat transfer between horizontal flat plates. *International Journal of Heat and Mass Transfer*, 9(8):803–817, 1966.
- [19] S Ostrach and Ya Kamotani. Heat transfer augmentation in laminar fully developed channel flow by means of heating from below. 1975.
- [20] Keisuke Fukui, Masamoto Nakajima, and Hiromasa Ueda. The longitudinal vortex and its effects on the transport processes in combined free and forced laminar convection between horizontal and inclined parallel plates. *International Journal of Heat and Mass Transfer*, 26(1):109–120, 1983.
- [21] HW Müller, M Lücke, and M Kamps. Transversal convection patterns in horizontal shear flow. *Physical Review A*, 45(6):3714, 1992.
- [22] K Fujimura and RE Kelly. Interaction between longitudinal convection rolls and transverse waves in unstably stratified plane Poiseuille flow. *Physics of Fluids*, 7(1):68–79, 1995.
- [23] PA Monkewitz and Ph Carrière. Convective Versus Absolute Instability in Mixed Rayleigh-Bénard-Poiseuille Convection. In *APS Division of Fluid Dynamics Meeting Abstracts*, pages Dg-01, 1997.
- [24] Rani Taher, Mohamed Mohsen Ahmed, Zoubida Haddad, and Cherifa Abid. Poiseuille-Rayleigh-Bénard mixed convection flow in a channel: Heat transfer and fluid flow patterns. *International Journal of Heat and Mass Transfer*, 180:121745, 2021.
- [25] E Schröder and K Bühler. Three-dimensional convection in rectangular domains with horizontal throughflow. *International journal of heat and mass transfer*, 38(7):1249–1259, 1995.
- [26] Mark E Braaten and Suhas V Patankar. Analysis of laminar mixed convection in shrouded arrays of heated rectangular blocks. *International journal of heat and mass transfer*, 28(9):1699–1709, 1985.
- [27] Hermann F Fasel, Fanlong Meng, Ehsan Shams, and Andreas Gross. CFD analysis for solar chimney power plants. *Solar energy*, 98:12–22, 2013.

- [28] Christian-Herbert Fischer, Nicholas A Allsop, Sophie E Gledhill, Tristan Köhler, Martin Krüger, Rodrigo Sáez-Araoz, Yanpeng Fu, Robert Schwieger, Johannes Richter, Peter Wohlfart, et al. The spray-ILGAR®(ion layer gas reaction) method for the deposition of thin semiconductor layers: Process and applications for thin film solar cells. *Solar Energy Materials and Solar Cells*, 95(6):1518–1526, 2011.
- [29] K Huang. Statistical mechanics 2nd edn, 1987.
- [30] Xiaoyi He and Li-Shi Luo. Theory of the lattice Boltzmann method: From the Boltzmann equation to the lattice Boltzmann equation. *Physical review E*, 56(6):6811, 1997.
- [31] Xiaoyi He and Li-Shi Luo. Lattice Boltzmann model for the incompressible Navier–Stokes equation. *Journal of statistical Physics*, 88(3):927–944, 1997.
- [32] Mohsen Eshraghi and Sergio D Felicelli. An implicit lattice Boltzmann model for heat conduction with phase change. *International Journal of Heat and Mass Transfer*, 55(9-10):2420–2428, 2012.
- [33] Theodore L Bergman, Frank P Incropera, David P DeWitt, and Adrienne S Lavine. *Fundamentals of heat and mass transfer*. John Wiley & Sons, 2011.
- [34] Iain G Currie. *Fundamental mechanics of fluids*. CRC press, 2016.
- [35] Salvatore P Sutera and Richard Skalak. The history of Poiseuille’s law. *Annual review of fluid mechanics*, 25(1):1–20, 1993.
- [36] Timm Krüger, Halim Kusumaatmaja, Alexandr Kuzmin, Orest Shardt, Goncalo Silva, and Erlend Magnus Viggén. The lattice Boltzmann method. *Springer International Publishing*, 10(978-3):4–15, 2017.
- [37] Anthony JC Ladd. Numerical simulations of particulate suspensions via a discretized Boltzmann equation. Part 1. Theoretical foundation. *Journal of fluid mechanics*, 271:285–309, 1994.

- [38] Anthony JC Ladd. Numerical simulations of particulate suspensions via a discretized Boltzmann equation. Part 2. Numerical results. *Journal of fluid mechanics*, 271:311–339, 1994.
- [39] Subrahmanyam Chandrasekhar. *Hydrodynamic and hydromagnetic stability*. Courier Corporation, 2013.
- [40] W. H. Reid and D. L. Harris. Some Further Results on the Bénard Problem. *The Physics of Fluids*, 1(2):102–110, 1958.